Optical Properties and Acoustic Phonon Dynamics of $Bi_2Sr_2CaCu_2O_{8+\delta}$ Crystals

by

© **Brad McNiven**

A thesis submitted to the School of Graduate Studies in partial fulfillment of the requirements for the degree of Master of Science.

Department of Physics & Physical Oceanography

Memorial University

May 2020

St. John's, Newfoundland and Labrador, Canada

Abstract

In this work, the optical properties and acoustic phonon behaviour of several $Bi_2Sr_2CaCu_2O_{8+\delta}$ (Bi-2212) superconducting crystals were investigated. Reflectance imaging on Bi-2212 crystals was first performed and along with Kramers-Kronig analysis, allowed for the extraction of the refractive index, extinction coefficient and both parts of the complex dielectric function. With these measured reflectances, a newly refined optical contrast method was presented and used in an attempt to obtain a secondary estimate of the refractive index and extinction coefficient of these crystals. Brillouin light scattering experiments were performed on Bi-2212 crystals at room temperature where six different acoustic modes were observed; the Rayleigh surface mode, two quasi-transverse bulk modes, the quasi-longitudinal bulk mode and two currently unknown modes. Using the peak frequency shifts and widths of the quasi-transverse and surface modes, the refractive index and extinction coefficient were extracted and used to calculate both parts of the complex dielectric function which were then compared to results found by reflectance analysis. The refractive index was then used to calculate the velocities of the three bulk modes and two unknown modes for angles ranging from approximately 3° to 21° from the [001] direction.

Acknowledgements

I would first like to extend a large thank you to my supervisors Todd Andrews and James LeBlanc for the opportunity of working on this project, your help guidance was essential in successfully completing it. I also extend another large thank you to Pat Clancy at McMaster University for providing the samples used in this work.

Next I would like to thank Dylan Goudie and Graham Layne for the help and insightful conversations on reflectance imaging and analysis, along with Gord Whelan for fabricating filter mounts used in our reflectance experiments.

Lastly I would like to thank my research group members Dillon Hanlon and Stephen Spencer along with my parents for help and encouragement throughout the duration of this project.

Table of contents

List of tables

List of figures

List of symbols

T_c	critical temperature
$\tilde{n}$	complex refractive index
n	real component of $\tilde{n}$
κ	imaginary component of $\tilde{n}$
λ	wavelength
R	reflectance
OC	optical contrast
Θ	phase
$\tilde{\epsilon}$	complex dielectric function
ϵ_1	real component of $\tilde{\epsilon}$
ϵ_2	imaginary component of $\tilde{\epsilon}$
σ	DC conductivity
$\mathbf{k}$	wavevector of photon
$\mathbf{q}$	wavevector of phonon
f	frequency shift
v_R	Rayleigh surface velocity
v_{LR}	longitudinal resonance velocity
v_T	quasi-transverse velocity
v_L	quasi-longitudinal velocity

Chapter 1

Introduction

1.1 Introduction to Superconductivity & Cuprates

To date, the mechanisms which give rise to high temperature superconductivity are some of the hardest questions still unanswered in physics. Since its discovery in the early 1900's, superconductivity has remained a highly studied field due to the potential applications in electronics and information storage and processing. For a material to be considered a superconductor, it must possess the following traits [6]. Firstly, there must be a state at which the electrical resistance goes to zero once reaching a critical temperature, T_c. Second, the superconductor must exhibit the Meissner effect, where magnetic field lines from the bulk are expelled when placed in a magnetic field.

Materials which exhibit the properties listed above are separated into two different types. Type I superconductors, sometimes referred to as elemental superconductors, are a class of materials known for their extremely low critical temperatures. Many of these metals exhibit temperatures on the millikelvin scale, such as titanium with $T_c = 0.39$ K [6]. Conversely, Type II superconductors consist of compounds which exhibit these superconducting properties that are much more complex in nature. These superconductors are known for being extremely difficult to study and as a consequence, much still remains unknown about their properties. Unlike Type I superconductors which only exhibit a superconducting phase below a critical magnetic field, Type II superconductors experience additional mixing of normal and superconducting states to a higher critical magnetic field. This is demonstrated in Fig 1.1, where a simplified

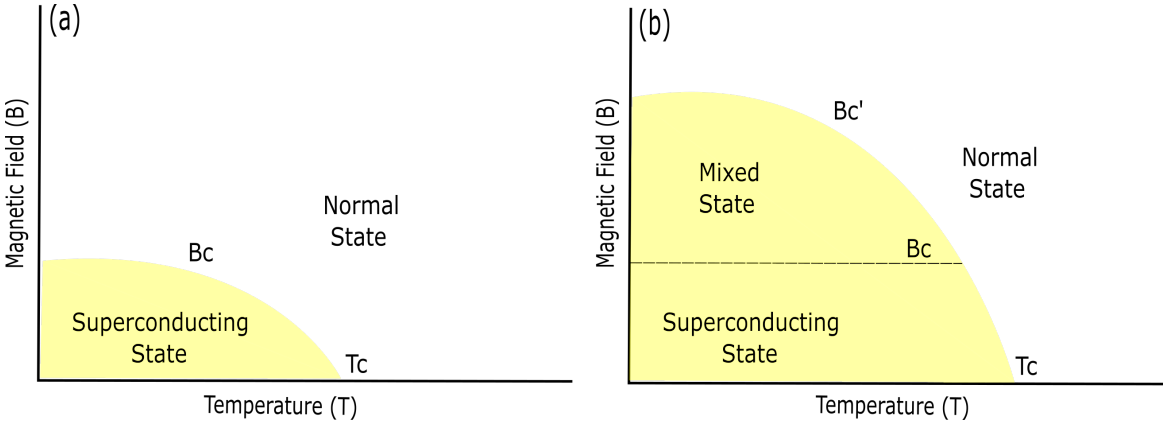

Figure 1.1: Schematic of the resulting phase diagram for (a) Type I and (b) Type II superconductors, where B is the magnetic field, B_c and B_c' are critical magnetic fields and T_c is the critical temperature.

phase diagram of both Type I and II superconductors is shown in Fig 1.1(a) and Fig 1.1(b), respectively. It is noted that in Fig 1.1(b), the superconducting state is cutoff at the same critical field B_c as in Fig 1.1(a), but additional mixing occurs above this threshold to a higher critical field B_c' and in turn, causes an increase in the critical temperature [6]. Type II superconductors have a T_c which exceeds the boiling point of liquid nitrogen (77 K) and for this reason are commonly referred to as high-T_c superconductors.

Within the group of high-T_c superconductors lies a sub-field of materials known as cuprates. Cuprates have highly anisotropic properties (e.g., electronic, elastic) and are layered compounds which are known for their unit cell containing at least one conducting CuO_2 plane, where the majority of electron movement happens parallel to the surface. These CuO_2 planes are separated from surrounding ones by a metallic atom and their presence is believed to be an important factor for the existence of superconducting states in cuprates as the resulting T_c has been found to be directly proportional to the number of CuO_2 planes found in the unit cell [26]. Cuprates are highly appealing for superconductivity studies due to their layered nature. These materials are effectively two dimensional superconducting planes contained in a three dimensional crystal which has made them highly sought after materials for two dimensional studies [38].

It is widely known that growing high quality cuprate crystals is exceptionally

difficult. These crystals are extremely brittle, highly influenced by their growth environment and in some cases are unstable when exposed to atmospheric conditions and for these reasons, synthesizing high quality crystals is notoriously difficult. Moreover, cuprate crystals experience severe grain boundary effects which act as impurities and ultimately impede many of the exotic states one is interested in when studying these materials [38].

1.2 Cuprate Phase Diagram

The critical temperature of a superconducting material is highly dependent on the level of doping. Doping is the act of deliberately introducing defects into the crystal which can be defined either as structural or chemical defects [38]. Doping causes a change in electronic density of states at the Fermi level, either introducing or removing possible electron states, resulting in either an underdoped or overdoped system, respectively. Structural defects are atoms introduced to the lattice which occupy either normally vacant lattice sites or interstitial sites where no atoms typically exist. Conversely, chemical defects refer to atoms being swapped from their original lattice sites. In the case of cuprates, these crystals are typically doped with oxygen. Fabricating a doped cuprate however is extremely nontrivial, as oxygen atoms are not uniformly spread out and will occupy any site which is accessible in the lattice [7]. This non-uniformity can result in major instabilities through the crystal and adds to the complexity of growing and reproducing cuprate crystals with a specific T_c.

Fig 1.2 presents a typical phase diagram for a cuprate where the doping parameter x indicates the level of oxygen doping per copper atom. Optimal doping occurs where the T_c is largest and in the case of cuprates is typically ~ 90 K ($x = 0.17$). Moreover, the superconducting state exists for $0.05 < x < 0.27$ and outside of these bounds the crystal exhibits an antiferromagnetic insulating phase when underdoped or a metallic phase when overdoped, complying to Fermi-liquid theory [17]. Above the superconducting dome resides two additional phases. The first is the pseudogap region, which is characteristic phase of a high temperature superconductor. The second is the strange metal phase, which is not fully described by Fermi-liquid theory [17].

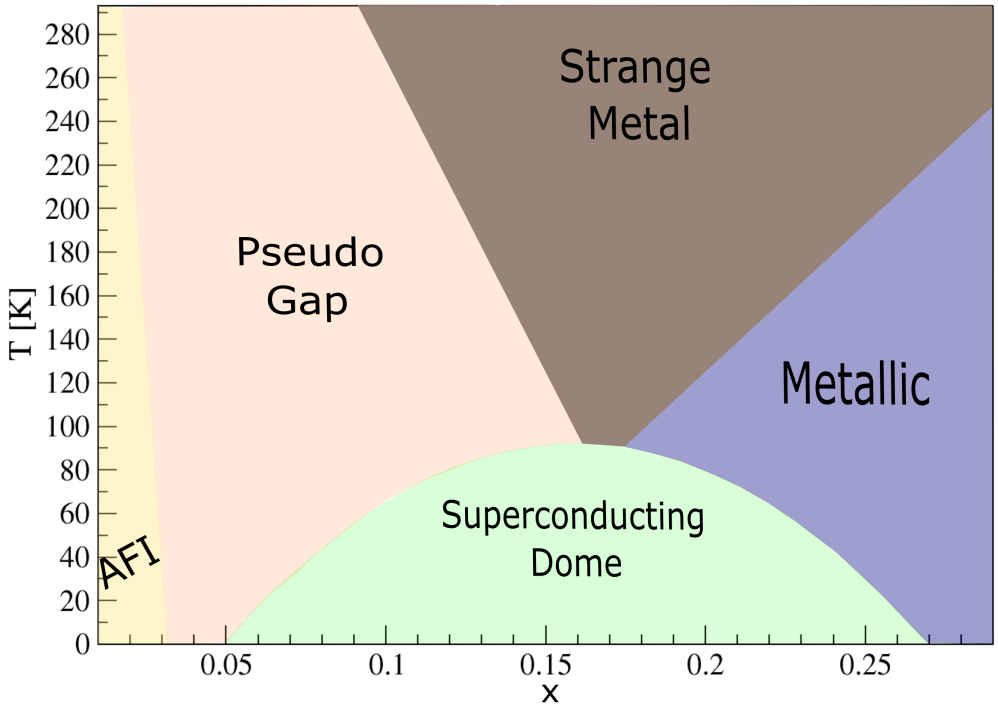

Figure 1.2: Phase diagram for a typical cuprate, where AFI corresponds to the antiferromagnetic insulating phase and x is the oxygen doping per copper atom.

1.3 $\mathbf{Bi_2Sr_2Ca_{n-1}Cu_nO_{2n+4+\delta}}$

$Bi_2Sr_2Ca_{n-1}Cu_nO_{2n+4+\delta}$, commonly referred to as BSCCO, is one of the most recognized cuprates and was the first high temperature superconductor discovered with no presence of rare earth elements [2]. BSCCO has three common crystal structures; Bi-2201, 2212 and 2223, which correspond to $n = 1, 2, 3$ in the chemical formula, respectively. In theory, BSCCO is one of the easiest cuprates to study as its strong bonding ensures the oxygen contained within the crystal is stable at room temperature [26]. Experimental studies, however report highly inconsistent results for bulk optical and mechanical properties.

Each of these three structures are layered crystals, however, several notable differences do exist. Bi-2201 and Bi-2223 are commonly doped with metals such as

lanthanum and lead. In the case of Bi-2223, these metal substitutions allow for the crystal to be more stable in atmospheric conditions for experimental analysis. Previous studies have been conducted on Bi-2212 doped with metals [11, 28, 35, 31, 44], however with an already highly stable crystal in atmospheric conditions, this is rarely done. Moreover, for this reason, along with its ease of growth compared to other BSCCO structures, Bi-2212 is the most studied structure to date. In this thesis, the Bi-2212 structure is studied and any mention of BSCCO assumes this structure unless otherwise stated.

Bi-2212 has a pseudo-tetragonal crystal structure which is shown in Fig 1.3, where $a \approx b = 0.542$ nm and $c = 3.09$ nm [9]. The unit cell is comprised of two semiconducting BiO planes, two insulating SrO planes and two charge carrying CuO_2 planes separated by a Ca^+ ion [26]. Bi-2212 is described as micaeous as its appearance is similar to that of mica and it also cleaves easily perpendicular the c-axis [38]. Each layer is separated by a BiO plane, where these planes are weakly bonded by Van der Waal forces. The presence of these weak bonds make Bi-2212 an ideal candidate for two-dimensional analysis as obtaining monolayer thick samples has been achieved by mechanical exfoliation techniques [43].

1.4 Previous Studies on Elastic Properties of Bi-2212

1.4.1 Brillouin Light Scattering

To date, three Brillouin light scattering experiments have been performed on BSCCO, with only the 2212 structure studied at room temperature [22, 27, 41]. Temperature dependent studies have not yet been performed using Brillouin light scattering as obtaining a reasonable signal has been a challenge due to poor sample quality.

The first reported spectra of Bi-2212 were presented by Baumgart *et al.* [27], where single crystals were investigated at 300 K. Due to poor quality crystals, only two modes were observed. The longitudinal surface resonance mode (LR) was seen at ~ 16 GHz and Rayleigh surface (R) modes at ~ 5 GHz. The resulting velocities were found to be $v_{LR} = 4650 \pm 300$ m/s and $v_R = 1525 \pm 150$ m/s, respectively, in an

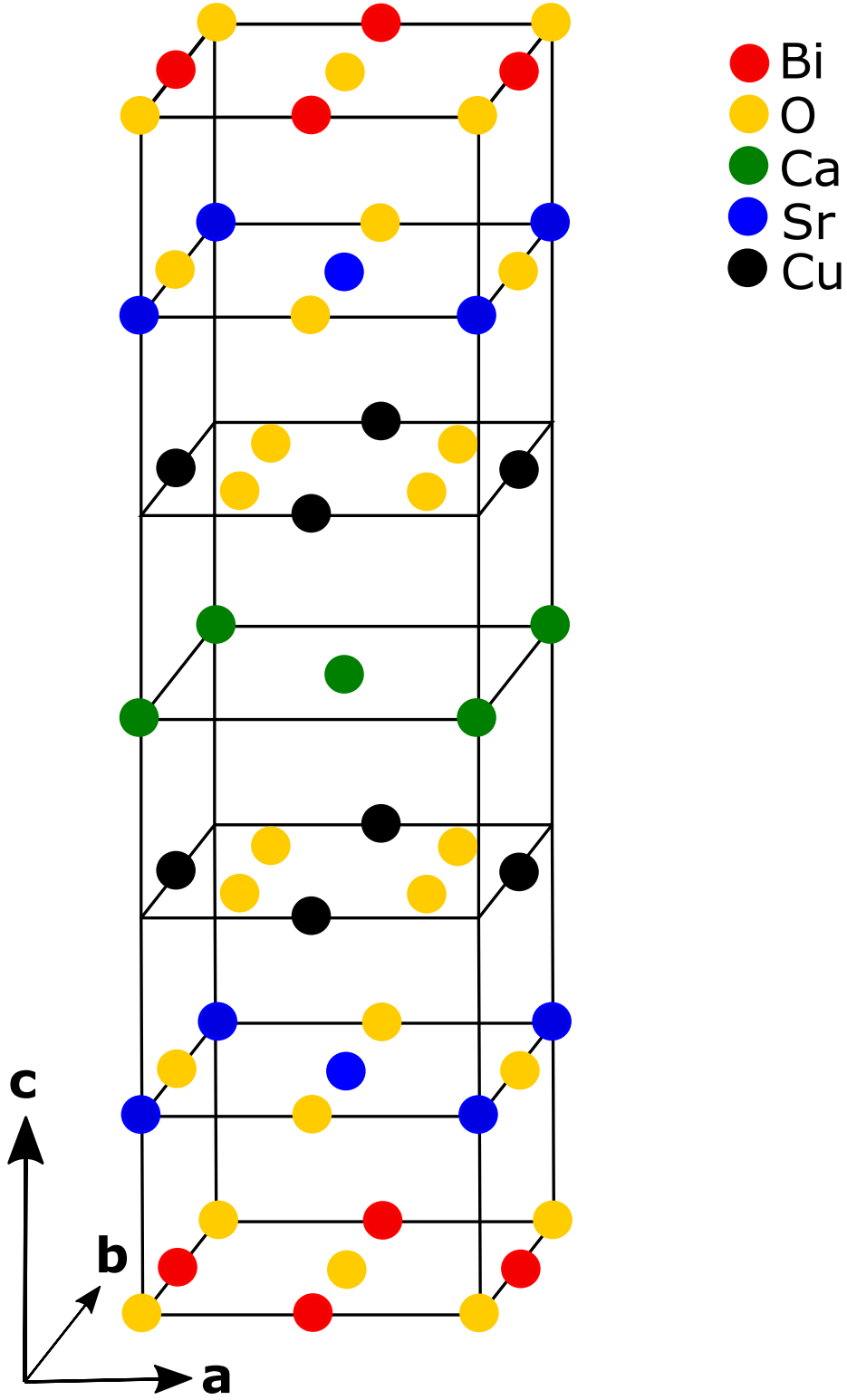

Figure 1.3: Unit cell for Bi-2212.

unspecified direction on the (001) plane.

A study published by Aleksandrov *et al.* [41] was centered on how different melt parameters in the crystal growing process affect the resulting surface wave velocity for single crystal Bi-2212. Here, stoichiometric ratios for bismuth, strontium, calcium and copper were varied between samples as was the cooling rate. The critical temperature of each of the three samples was measured and ranged between 10 K and 88 K. Brillouin light scattering was performed on the (001) plane of each sample, where the average surface wave velocity was found to be 1560 m/s and 1310 m/s for the [100] and [010] directions, respectively.

The most recent study on Bi-2212 using Brillouin light scattering was conducted by Boekholt *et al.* in 1991 [22]. Bi-2212 single crystal samples were grown using the self-flux method with T_c ranging between 78 K and 92 K and were probed at various directions on multiple crystallographic planes. With angles ranging between $0° - 75°$ away from the [110] direction on the (001) plane, four modes were observed; the Rayleigh surface, longitudinal resonance and two bulk transverse modes, with the Rayleigh surface and longitudinal resonance velocities determined to be 1540 ± 66 m/s and 4386 ± 184 m/s, respectively. Angles ranging between $0° - 75°$ away from the [110], [100] and [010] directions were also probed on the (001) plane and no change was seen in both the Rayleigh and longitudinal resonance velocities.

The [001] and [100] directions were also probed on the (010) plane. In the first case, only the Rayleigh, longitudinal resonance and one bulk transverse mode were observed. The Rayleigh and longitudinal resonance sound velocities were calculated to be 1508 ± 76 m/s and 3413 ± 212 m/s, respectively. In the second case, all four modes were seen again and the Rayleigh and longituidnal resonance velocities were determined to be 1396 ± 97 m/s and 4380 ± 194 m/s, respectively.

By assuming the longitudinal resonance velocity is approximately equal to the longitudinal velocity, the five independent elastic constants for Bi-2212 were calculated assuming hexagonal symmetry with cylindrical symmetry along the c-axis. With these assumptions, and using peak frequency shifts obtained by Brillouin light scattering, the elastic constants were found to be $c_{11} = 125 \pm 10$ GPa, $c_{33} = 76 \pm 9$ GPa, $c_{12} = 79 \pm 7$ GPa, $c_{13} = 56 \pm 6$ GPa and $c_{44} = 16 \pm 1$ GPa. With the Rayleigh surface velocity calculated, its associated elastic constant was determined to be $c_R = 15.4$ GPa.

1.4.2 Ultrasonic Measurements

Several ultrasonic studies have been published on Bi-2212 with a focus on either measuring the acoustic velocities or studying the temperature dependence on elastic behaviour [3, 5, 15, 16, 20, 24, 44, 45, 46]. Further ultrasonic experiments had been performed on Bi-1113 [11], Bi-2223 [44], and Bi(Pb)-2212 [28, 31, 35], however the following discussion is restricted to Bi-2212.

Ultrasonic measurements were conducted on single crystal Bi-2212 samples with $T_c = 84.5$ K by Wang *et al.* [45, 46]. Longitudinal sound waves were propagated along both the [100] and [010] directions as the sample was cooled from 280 K to $\sim$ 8 K and then heated back up to its initial temperature of 280 K. For longitudinal waves propagating along [100], it was determined that the longitudinal velocity at room temperature was $\sim$ 4580 m/s before cooling and after reheating to 280 K. A thermal hysteresis was observed between 250 K $-$ 280 K and was attributed to a displacive first order phase transition. Discontinuities were also observed in the velocity vs temperature curves at 90 K and 150 K which were labelled as anomalous phase-like transitions. With longitudinal waves propagating along [010], a slight difference was observed in the thermal hysteresis, with monotonic behaviour upon cooling and heating. Initially, the longitudinal velocity at room temperature was measured to be $\sim$ 4130 m/s and once cooled and reheated, decreased to $\sim$ 4100 m/s. Shear waves were also measured which were propagated along the [010]. The velocity was measured to be $\sim$ 2460 m/s at 280 K and while cooling, three anomalous discontinuities appeared at 250 K, 150 K and 90 K in the velocity vs temperature curves.

Ultrasonic studies were also performed by Wu *et al.* [15, 16] on flux grown Bi-2212 single crystals to study how elasticity varies with temperature. Longitudinal sound velocities were measured along the [100], [010] and [110] directions and were found to be 4320 m/s, 4097 m/s and 4647 m/s, respectively, at 250 K. With shear waves propagated along the [010] direction, the velocity was also measured and found to be 2762 m/s at 250 K. Measured velocities were used to determine the elastic constants assuming an orthorhombic crystal structure and were found to be $c_{11} = 123$ GPa, $c_{12} = 67$ GPa, $c_{22} = 111$ GPa and $c_{66} = 50$ GPa at 250 K. Additionally, the in plane shear mode elastic constant (c') as well as the longitudinal elastic constant for waves propagating along the [110] direction (c_L) were measured to be 25 GPa and 143 GPa, respectively. For c_{11} and c_{22}, stiffening was observed as temperature

was decreased and three minima were present at 100 K, 140 K and 240 K in the velocity *vs* temperature curves for c_{66}. These minima were also observed in c' and were attributed to structural instabilities caused by geometric misfit layers which repeatedly stack upon one another. Similar structural phenomena has been seen in other high temperature superconductors above T_c such as $YBa_2Cu_3O_{7-x}$ (YBCO) [14], however the origin of these anomalies remains unknown.

Further ultrasonic studies of the temperature dependence of the elastic properties on single crystal Bi-2212 were carried out by Saint-Paul *et al.* [24], where shear and longitudinal waves along were propagated along the [001] direction to study the effects of temperature change on c_{44} and c_L. The resulting longitudinal velocity was measured to be $\sim$ 5000 m/s and similar discontinuities as reported previously [15, 16], were observed at 110 K, 190 K and 250 K in c_{44}.

Similar anomalous discontinuities were also observed in temperature dependent velocity curves by He *et al.* [44], where an unknown transition was measured at 200 K in single crystal Bi-2212 crystals. Using ultrasonic techniques, the longitudinal and transverse velocities were measured at room temperature to be 2846 m/s and 1735 m/s, respectively. Moreover, the longitudinal, shear, bulk and Young's moduli at room temperature were found to be 43.4 GPa, 16.1 GPa, 21.9 GPa, and 38.8 GPa, respectively.

Polycrystalline ceramic Bi-2212 samples with $T_c = 74$ K were investigated by Sihan *et al.* [20] using ultrasonic techniques. Samples were cooled to $\sim$ 10 K and heated back up to $\sim$ 300 K where a thermal hysteresis was again observed. The longitudinal sound velocity was initially measured to be 2847 m/s at room temperature and after reheating had increased slightly to 2855 m/s. From the propagated shear waves, the shear sound velocity was measured to be $\sim$ 1740 m/s at room temperature before and after cooling. To take into account the porosity in ceramic Bi-2212 samples, velocities were corrected by theoretical modelling which yielded 3110 m/s and 1900 m/s for the longitudinal and shear sound velocities, respectively. Temperature dependence of Poisson's ratio as well as the bulk, Young's and shear moduli was also investigated, where anomalies at $\sim$ 200 K and $\sim$ 80 K were observed in both Young's and shear moduli.

Dense, polycrystalline samples were also studied by Chu *et al.* [3], where Bi-2212 powders were formed into bulk samples by hot isostatic pressing and sinter forging

techniques. It was noted that samples created by hot isostatic pressing were found to be 100% dense while those created by sinter forging were $90 - 95\%$ dense. Ultrasonic measurements were carried out with longitudinal and transverse waves propagated in unspecified directions. For samples prepared by hot isostatic pressing, the longitudinal and one transverse velocity were measured to be 2464 m/s and 1710 m/s, respectively. In a separate, unspecified direction, the longitudinal and two transverse velocities were measured as 3986 m/s, 1699m/s, and 2422 m/s, respectively. Similarly, for samples prepared by sinter forging, the longitudinal and one transverse mode were measured to be 3330 m/s and 1968 m/s, respectively, in one direction, while the longitudinal and two transverse modes in another direction were found to be 4024 m/s, 1956 m/s, and 2311 m/s, respectively.

Most recently, focus on acoustics and elastic behavior of Bi-2212 was performed by Chang *et al.* [5], where dense, highly textured ceramics produced by sinter forging were probed by propagating longitudinal and shear waves at 290 K. In an unspecified direction, the longitudinal and shear sound velocities were measured to be 2670 ± 10 m/s and 1750 ± 10 m/s, respectively. Along another unspecified direction, one longitudinal mode and two shear modes were observed with sound velocities measured as 4370 ± 10 m/s, 2460 ± 10 m/s and 1740 ± 10 m/s, respectively. From these longitudinal velocities, the elastic stiffness within the (001) layers was assumed to be much larger than the stiffness between the layers. Temperature dependence was also investigated, where velocities were found to be monotonic and no anomalous behavior or hysteresis was observed upon heating or cooling.

1.5 Literature on the Optical Properties of Bi-2212

To obtain the bulk acoustic phonon velocities from Brillouin light scattering spectra, one needs the refractive index of the material being investigated. In the case of Bi-2212 crystals, much remains unknown regarding its optical properties, particularly in the visible light region.

Experimental reflectance and ellipsometric data was obtained on Bi-2212 single crystals by Bozovic [1] to study acoustic plasmons. Spectra were collected from $0 \sim 44,000$ cm^{-1} where Kramers-Kronig transformations were applied to resulting spectra to obtain both real and imaginary parts of the complex dielectric function as well as

the real part of the optical conductivity. It was noted that any optical constants calculated by this method should be treated as estimates, especially for cuprates as they appear non Drude-like [25]. Because of this, a correction was performed on both parts of the complex dielectric function where changes were reported to range between $15 \sim 30\%$ in YBCO, another high-temperature cuprate. Furthermore, it was speculated that with cuprates agreeing with the layered electron gas model over the Drude model, it is likely there exists multiple acoustic plasmon branches.

A separate study performed by Sandilands *et al.* [19] focused on collecting reflectance and transmittance spectra on Bi-2212 crystals to investigate any changes due to sample thickness. Sample thicknesses ranged from bulk thickness down to 12 nm and transmittance and reflectance spectra were collected up to $\sim 5,000$ cm^{-1}. It was seen that the transmittance ratio between sample and substrate increased with decreasing thickness while the reflectance ratio decreased with decreasing thickness. Over this frequency range, the real parts of dielectric function and optical conductivity were obtained, where Drude-like behaviour was observed only in Bi-2212 samples with thicknesses less than 123 nm. Moreover, in samples < 16 nm in thickness, the real part of the optical conductivity was found to be flat and the real part of the dielectric function was positive over the entire frequency range; behaviour indicative of the samples being fully insulating.

Reflectance measurements were also conducted on Bi-2212 crystals by Hwang *et al.* [12], where mulitple samples with a T_c ranging from 60 K $-$ 96 K were studied to determine the doping and temperature dependence on various optical properties, including the optical conductivity. Reflectance spectra were collected on the (110) plane of samples with a frequency ranging from $0 - 5,000$ cm^{-1}, where both temperature and doping were shown to have a noticeable impact on resulting spectra, particularly for overdoped samples. After Kramers-Kronig transformations, the optical conductivity was shown as a function of frequency, where significant temperature and doping dependence was seen only for frequencies $< 3,000$ cm^{-1}. Moreover, the amplitude of the optical conductivity was also inspected, where there was little temperature or doping dependence observed in frequencies $> 1,000$ cm^{-1}.

The reflectance along both a and b axes of Bi-2212 crystals was explored by Quijada *et al.* [21]. Reflectance measurements at room temperature were collected from Bi-2212 crystals with a frequency range up to $30,000$ cm^{-1}. The resulting reflectance

function appeared the same for both axes below $10,000$ cm^{-1}, however above this frequency the reflectance began to deviate between the two axes with increasing frequency. By Kramers-Kronig transformation, the optical conductivity was obtained as a function of frequency and the resulting conductivity in both axes was found to be the same below $25,000$ cm^{-1}.

An experimental and theoretical approach was taken by Kobayashi *et al.* [13] to study the birefringence and optical properties of Bi-2212 crystals. A high-accuracy universal polarimeter (HAUP) was used to explore the dependence of gyration, linear dichroism, retardation and birefringence on temperature. With the temperature decreased from 300 K to < 10 K, there was no change seen in either the extinction coefficient birefringence or linear dichroism, however below T_c, a decrease in both retardation and refractive index birefringence was seen. Conversely, the g_{33} component of the gyration tensor and ellipticity were seen to sharply increase below T_c. It is noted that these findings do not coincide with those obtained previously by either Kramers-Kronig transformation or reflectance measurements. It was suggested that this disagreement was a direct result of neglecting the structural phase transitions seen above T_c in velocity versus temperature curves obtained by ultrasonic measurements [15, 16, 24, 45, 46].

1.6 Motivation & Present Work

It is well known that bulk high-temperature superconductors are dominated by electron-electron coupling, however it is unclear if and how this coupling changes as sample thickness is decreased. Moreover, with minimal work published on the acoustic phonon behavior on bulk Bi-2212 crystals, there is yet to be a baseline established on what to expect for these bulk materials as well as other closely related materials (such as YBCO).

In this work, the optical and elastic properties of three bulk Bi-2212 samples with critical temperatures of 78 K, 90 K and 91 K were studied. With large advancements made in crystal growing since publication of the latest acoustic study almost thirty years ago, this work aimed to both supplement and complement existing elastic data.

To determine the bulk acoustic phonon velocities from Brillouin spectra, the refractive index of Bi-2212 was first needed. With no reliable literature containing this

information, reflectance imaging on each of the three samples was performed and through use of Kramers-Kronig transformations, the refractive index along with the extinction coefficient and real and imaginary parts of the dielectric function were extracted at a wavelength of 532 nm. A refined optical contrast method used to extract the refractive index and extinction coefficient of a thin crystalline sample deposited onto a semiconducting layer was also presented along with preliminary results for these constants with bulk Bi-2212 crystals attached to carbon tape and aluminum.

Brillouin light scattering experiments were conducted at room temperature on two samples of Bi-2212 at a wavelength of 532 nm. A surface mode, three bulk modes and two currently unknown modes were observed and using relations between acoustic mode frequency shifts, another estimate of the refractive index and extinction coefficient for Bi-2212 was obtained and compared with those found by other methods listed above. The refractive index along with collected peak frequency data was used to calculate the bulk acoustic phonon velocities for phonons travelling $3^\circ \sim 21^\circ$ from the [001] direction.

The remainder of this thesis is organized in the following manner. Chapter two presents the characterization and preparation of the three Bi-2212 samples used in this work. Chapter three is dedicated to a reflectance study of Bi-2212, where collected reflectance images are presented along with the analyses of these images and the extracted optical constants by two separate methods. Chapter four is dedicated to Brillouin light scattering, where collected spectra of multiple samples are shown and are ultimately used to extract the optical constants and acoustic phonon velocities. Chapter five provides some concluding remarks and suggests future work still left to be done on this project.

Chapter 2

Bi-2212 Samples

The Bi-2212 samples used in this work have transition temperatures of 78 K, 90 K, and 91 K and were obtained from Dr. Pat Clancy from McMaster University. Samples with T_c=78 K were grown by the flux growth method, where each element used to form Bi-2212 are dissolved in a solvent which is subject to extremely high temperature allowing crystallization to occur over time [23]. The crystallization of Bi-2212 single crystals are a result of such reactions when specific stoichiometric ratios of each metal are combined, however the overall crystallinity of Bi-2212 samples with $T_c = 78$ K is unknown. The two remaining Bi-2212 samples studied in this work are known to be single crystal, however the sample growth method remains unknown. Moreover, each Bi-2212 crystal studied is noted to be highly opaque.

Fig 2.1 presents an image of the parent Bi-2212 crystal with $T_c = 78$ K and throughout this work is referenced as sample TC78. This crystal had dimensions $10 \times 3 \times 2$ mm^3 and both reflectance and Brillouin scattering experiments were conducted on pieces of TC78 removed from the parent sample shown. From the figure, it is clear that TC78 is highly irregular when compared to a typical layered Bi-2212 crystal. Its appearance is not planar as one would expect and due to this, any layers exfoliated from the bulk were crumbly. The pieces removed from the parent crystal for experimental purposes had approximate dimensions $1 \times 1 \times 0.5$ mm^3 and one surface was exfoliated with adhesive tape in an attempt to make one surface as flat as possible to maximize the quality of Brillouin and optical reflectance signals.

Fig 2.2 shows the parent Bi-2212 crystal with T_c=91 K, where its dimensions were $10 \times 2 \times 0.05$ mm^3. This sample is labelled as TC91 and exhibited highly planar

Figure 2.1: Parent Bi-2212 sample with $T_c = 78$ K.

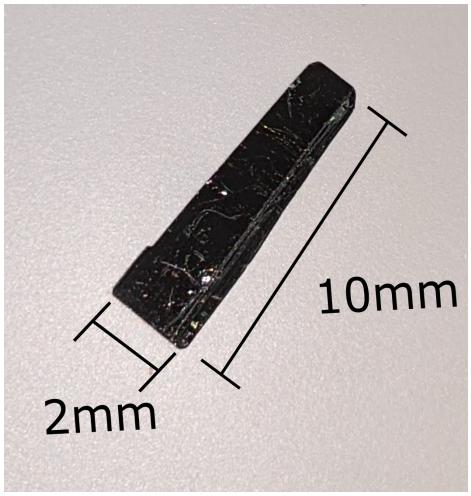

Figure 2.2: Parent Bi-2212 sample with $T_c = 91$ K.

structure by cleaving easily perpendicular to the [001] direction. In contrast to TC78, these samples exfoliated well with adhesive tape and the result is a thinner, structured crystal which were taken advantage of in reflectance experiments. Samples removed from the parent crystal for experimental work had dimensions $10 \times 2 \times 0.02$ mm^3.

The Bi-2212 crystal with T_c=90 K is referred to as sample TC90. The parent crystal looked almost identical to that shown in Fig 2.2, with a highly planar structure and cleaved easily perpendicular to the [001] direction. The only notable difference between TC90 and TC91 was the crystal size, with TC91 samples used in experiments being $2 \times 1 \times 0.05$ mm^3.

Table 2.1: Bi-2212 sample properties and physical characteristics for the crystals used in reflectance and Brillouin scattering experiments.

Sample Name	Tc (K)	Dimensions (mm^3)	Growth Method	Crystallinity	Layered
TC78	78	$1 \times 1 \times 0.5$	Flux	Irregular	No
TC91	91	$10 \times 2 \times 0.02$	Unknown	Planar	Yes
TC90	90	$2 \times 1 \times 0.05$	Unknown	Planar	Yes

Table 2.1 provides a summary of the key characteristics of each of the three samples studied in this work, where the dimensions correspond to the size of samples used in both reflectance and Brillouin scattering experiments obtained from the parent samples described and shown above.

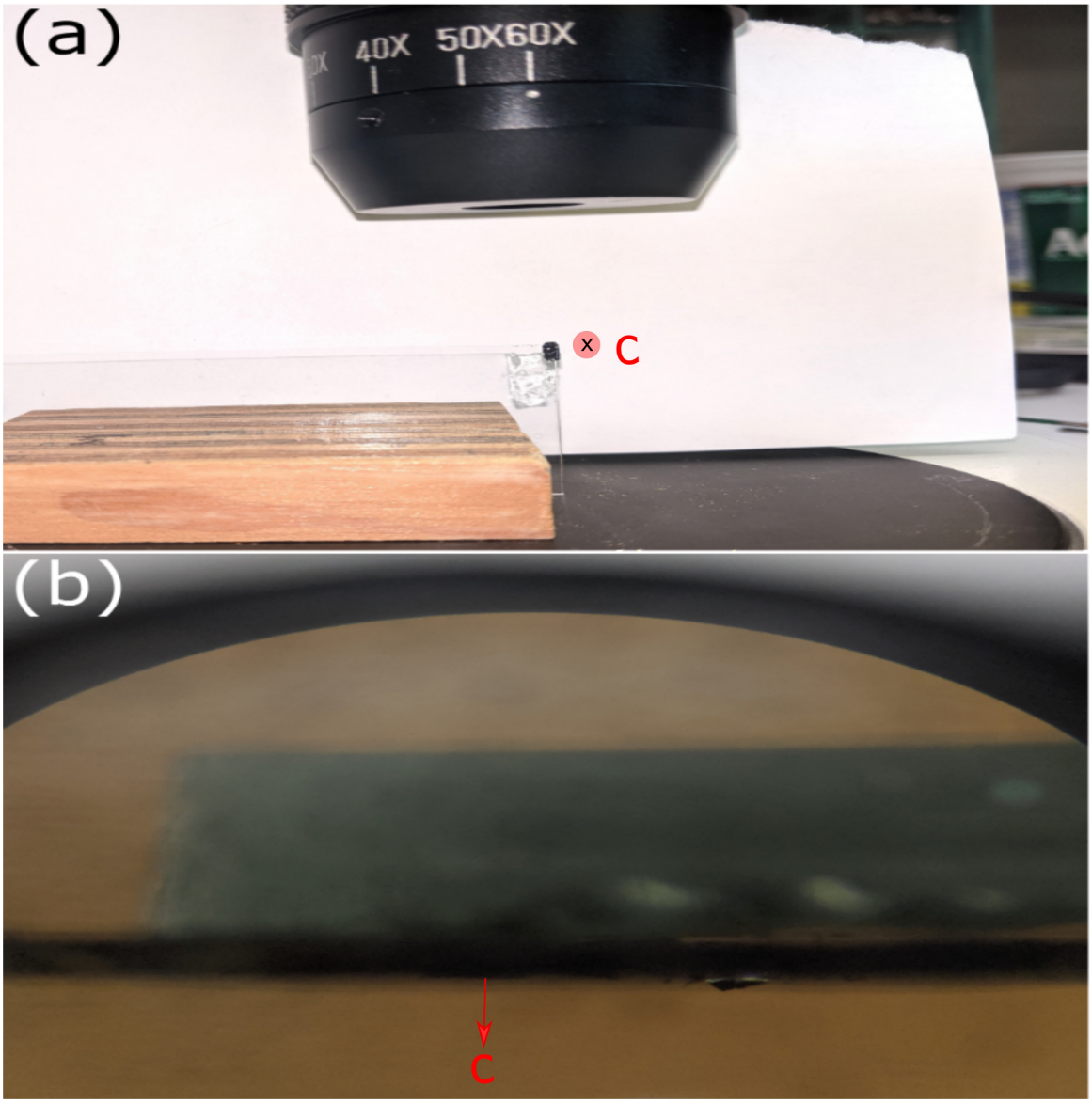

Figure 2.3: Image showing the process to gauge planarity of Bi-2212 crystals. The c-axis is indicated. (a) Sample orientation to obtain sample image (b) Resulting image, where the distance between the bottom of the sample and top of the microscope slide was measured across the length of the sample to observe any non-uniformity in sample thickness.

The planarity of the samples studied is quite important as the overall flatness of the probed surface can have an impact on the quality and signal of collected Brillouin spectra and reflectance images. As discussed above, samples TC90 and TC91 are layered, however it was unknown whether layers were stacked purely in the [001]

direction or if the layering occurred at a slight angle. To test this, a small sample of each of the two samples was mounted to the end of a microscope slide as shown in Fig 2.3(a). Each sample was then imaged on two sides to check for thickness changes over the length of the sample (see Fig 2.3(b)). The thickness deviation was $\sim 5\%$ over the entire length of each, indicating high uniformity for layer stacking. As mentioned, TC78 crystals were highly irregular and did not easily exfoliate, but attempts were made to remove any jagged or extruding pieces before mounting onto a stage prior to experiments.

Chapter 3

Reflectance Imaging Methods & Optical Constants of Bi-2212

3.1 Theory

3.1.1 Multilayer Interference & Optical Contrast

When a sample whose optical properties are to be determined is deposited onto a substrate, one typically uses Fresnel's multilayer interference relations to mathematically describe this layered system [4]. A schematic of such a system is presented in Fig 3.1, where the sample and underlying substrate are separated by an oxide layer. Usually substrates used in these types of analyses are semiconductors and the surfaces of these substrates will oxidize, so during the manufacturing process an oxide layer with a precise thickness is added. In Fig 3.1, it is noted that light will reflect differently due to a change in optical path length caused by reflection and transmission at each of the boundaries for the air-oxide-substrate and air-sample-oxide-substrate systems. The substrate is treated as a semi-infinite layer where no reflection will occur from its bottom interface once light has transmitted inside. This is because the optical penetration depth ($OPD = \lambda/4\pi\kappa$) for light with $\lambda = 532$ nm into crystalline silicon is on the order of 1 μm and this is much less than the thickness of the silicon substrate.

Mathematically, the reflections between both the substrate and sample-substrate systems can be described through Fresnel's equations for multilayer interference. The

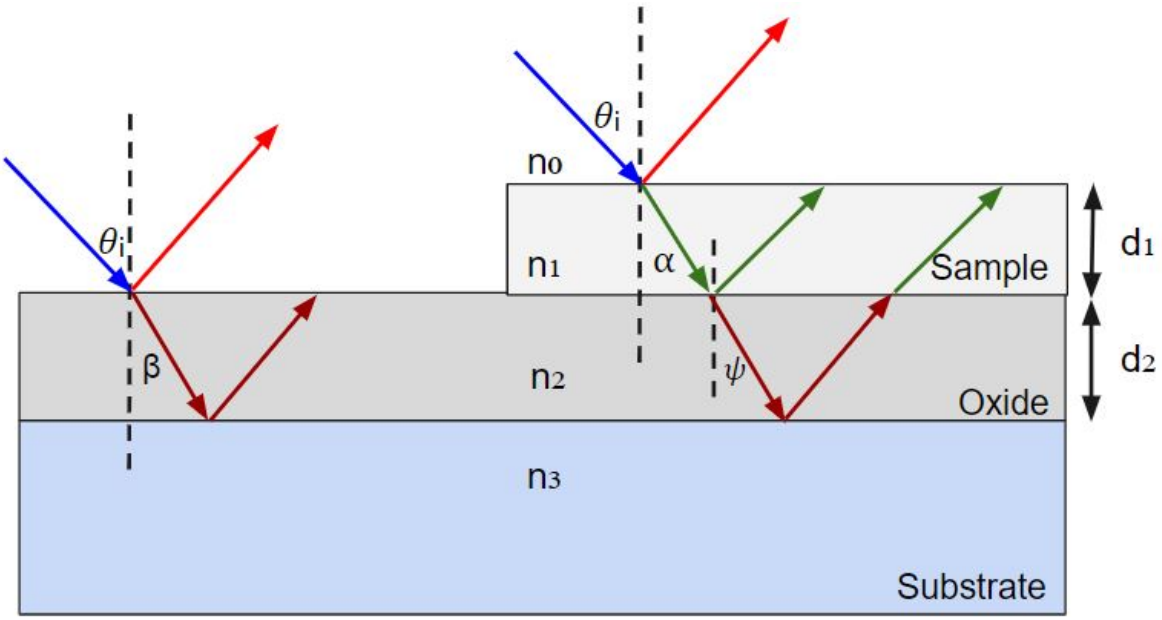

Figure 3.1: Multilayer system for sample deposited on a susbstrate with an oxide layer. n_i - refractive index of the medium, θ_i - incident angle, d_i - thickness of the sample or oxide layer and α, β, Ψ - refracted angle of each interface.

ratio of reflected and incident electric fields is known as the reflection coefficient and for the air-substrate-oxide system is defined by [4]

$$r_{substrate} = \frac{r_{02} + r_{23}e^{-2i\phi_2}}{1 + r_{02}r_{23}e^{-2i\phi_2}}. \tag{3.1}$$

Likewise, the reflection coefficient for the air-sample-oxide-substrate system is [4]

$$r_{sample} = \frac{r_{01} + r_{01}r_{12}r_{23}e^{-2i\phi_2} + r_{12}e^{-2i\phi_1} + r_{23}e^{-2i(\phi_1+\phi_2)}}{1 + r_{12}r_{23}e^{-2i\phi_2} + r_{01}r_{12}e^{-2i\phi_1} + r_{01}r_{23}e^{-2i(\phi_1+\phi_2)}}. \tag{3.2}$$

Here, r_{ij} are the reflection coefficients for layers i and j and are defined by

$$r_{ij} = \frac{\tilde{n_i} - \tilde{n_j}}{\tilde{n_i} + \tilde{n_j}}, \tag{3.3}$$

where $\tilde{n}$ is the complex refractive index $\tilde{n} = n + i\kappa$, with n and κ being the refractive index and extinction coefficient, respectively. Furthermore, ϕ_i is the phase difference

for the i^{th} layer and is given by

$$\phi_i = \frac{2\pi \tilde{n}_i d_i \cos\theta_i'}{\lambda}, \tag{3.4}$$

where θ_i' is the angle of refraction.

From the reflection coefficients, the reflectance for the substrate is given by

$$R_{substrate} = |r_{substrate}|^2, \tag{3.5}$$

and similarly for the sample,

$$R_{sample} = |r_{sample}|^2. \tag{3.6}$$

With the reflectance for both the substrate and sample, the optical contrast can then be calculated. Optical contrast is a renormalization of the difference in contrast between the sample and substrate with respect to the substrate. The optical contrast is defined as

$$OC = \frac{R_{substrate} - R_{sample}}{R_{substrate}}. \tag{3.7}$$

3.1.2 Kramers-Kronig Relations

The Kramers-Kronig (KK) relations are a set of mathematical functions which link the real and imaginary components of a complex response function [8]. These relations are used to determine the complex refractive index. Both n and κ are frequency dependent and can be calculated via

$$\begin{aligned} n(\omega) &= \frac{1 - R(\omega)}{1 + R(\omega) - 2\sqrt{R(\omega)}\cos\Theta(\omega)}, \\ \kappa(\omega) &= \frac{2\sqrt{R(\omega)}\sin\Theta(\omega)}{1 + R(\omega) - 2\sqrt{R(\omega)}\cos\Theta(\omega)}, \end{aligned} \tag{3.8}$$

where $R(\omega)$ and $\Theta(\omega)$ are the reflectance and phase at a specific frequency. Both n and κ are related through $\Theta(\omega)$, which can be found by evaluating

$$\Theta(\omega) = \frac{\omega}{\pi} \int_0^\infty \frac{\ln R(\omega') - \ln R(\omega)}{\omega^2 - \omega'^2} \mathrm{d}\omega'. \tag{3.9}$$

Although the KK relations only provide estimates, if one can determine $\Theta(\omega)$, any optical constants of interest can be estimated [1], such as the real (ϵ_1) and imaginary (ϵ_2) components of the dielectric function

$$\begin{aligned} \epsilon_1(\omega) &= n(\omega)^2 - \kappa(\omega)^2, \\ \epsilon_2(\omega) &= 2n(\omega)\kappa(\omega), \end{aligned} \tag{3.10}$$

or the real component of the DC conductivity

$$Re(\sigma(\omega)) = \frac{4\pi\epsilon_2(\omega)}{\omega}. \tag{3.11}$$

3.2 Experimental Setup

Typically, if one is interested in obtaining sample images on the micrometer level or below, it is common to use characterizing tools such as scanning tunneling microscopy (STM), atomic force microscopy (AFM), scanning electron microscopy (SEM) or transmission electron microscopy (TEM). While these tools are undoubtedly powerful, there are several hindrances which can make certain analyses quite difficult. From a sample perspective, these methods can be largely destructive and typically are unable to probe large sample areas efficiently, a necessary criteria for obtaining layering in deposited samples.

Optical contrast microscopy (OCM) is a new method being used for thickness characterization [4], however it has the potential for observing topographic information and surface defects. Its highly simplistic nature when compared to other imaging methods makes it a promising technique for future thin film studies. OCM is extremely quick and most importantly, a non-destructive method for obtaining sample images with the ability of probing large surfaces.

Fig 3.2 presents a schematic of a typical OCM setup. A white light source is used as the light source, which passes through a bandpass filter and then reaches a beam splitter. From here, light is reflected 90° and passes through a lens which focuses the light onto a sample deposited on a substrate. At this stage, light that is incident

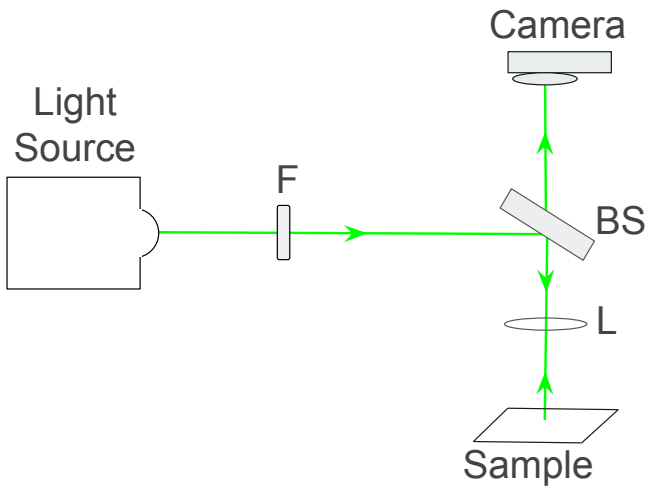

Figure 3.2: Schematic for an optical contrast microscopy setup where F - bandpass filter, BS - beam splitter and L - lens.

on both the substrate and sample-substrate regions is back reflected, where it passes back through the beamsplitter and is collected by a camera positioned directly above. Geometry is highly important when performing OCM. By having the incident beam impinge upon the sample at normal incidence, Eqns 3.1-3.2 become simplified by removing any dependence on the incident angle in Eqn 3.4 as well as the polarization of the incident beam.

Fig 3.3 shows the Leica DMLP reflecting microscope used to obtain reflectance images on Bi-2212 crystals in this work. A 12 V power supply was used with an output power ranging from $10 - 12$ V to power a broadband Philips halogen lamp. The light first passed through a 532 ± 10 nm bandpass filter, where the beam was then reflected 90° to a set of objectives, which provided either 5x, 10x, 20x or 50x magnification. The light was then focused onto the sample below by the objective, which was back reflected and collected by a Lumenera Infinity 1 camera. The image was then displayed on a computer screen using the Infinity 1 software.

The resulting image of the sample displays the intensity of reflected light for each pixel through the red, green, and blue color channels. With the reflectance of both the substrate and sample being the ratio of measured intensity with the total intensity,

Figure 3.3: Leica DMLP reflection microscope.

Eqn 3.7 may be rewritten as

$$OC = \frac{I_{sub} - I_{sample}}{I_{sub}}, \tag{3.12}$$

where I_{sub} and I_{sample} refer to the intensity due to the substrate and sample boundaries, respectively.

3.3 The RGB Color Model

The color one sees is not a characteristic of a given material, rather how the brain perceives the reflection, transmission or absorption of energy [29]. For this reason, various color spaces have been created which allow for color to be analyzed for specific digital processing purposes. The International Commission on Illumination (CIE)

color space is one of the most widely used as it encompasses the RGB color model, a model used in almost all technology using digital output and display screens. This model works using the three primary colors, red (R), green (G), and blue (B) and adjusting each of the three colors to output specifically desired colors.

Mathematically, one may determine each RGB value by first calculating each point in the XYZ color space, [10, 42]

$$\begin{aligned} X(\lambda) &= \int_0^\infty \bar{x}(\lambda)P(\lambda)R(\lambda,\theta_i)d\lambda, \\ Y(\lambda) &= \int_0^\infty \bar{y}(\lambda)P(\lambda)R(\lambda,\theta_i)d\lambda, \\ Z(\lambda) &= \int_0^\infty \bar{z}(\lambda)P(\lambda)R(\lambda,\theta_i)d\lambda, \end{aligned} \tag{3.13}$$

where X, Y and Z correspond to the three tristimulus values and $P(\lambda)$ is the spectral power distribution, $R(\lambda,\theta_i)$ is the reflectance and $\bar{x},\bar{y},\bar{z}$ are the color matching functions. From here, RGB values are determined through the transformation [10]

$$\begin{bmatrix} R \\ G \\ B \end{bmatrix} = \begin{bmatrix} X \\ Y \\ Z \end{bmatrix} \Big[M_d\Big]^{-1}, \tag{3.14}$$

where $[M_d]$ is a device dependent transformation matrix. This matrix is constructed by using the values corresponding to white light from the tristimulus values along with the sets of coordinates from $\bar{x},\bar{y}$ and $\bar{z}$ which correspond to R, G, and B based on the monitor used to display the image [10].

In the RGB color model, there is an associated 8 bit color channel for the colors red, green and blue, yielding 256 (2^8) possible color channels. By considering each R,G,B channel, a total of $16,777,216$ (256^3) possible color combinations exist. This can be seen in the simplified example presented in Fig 3.4. For red, green, and blue, the RGB matrix is $(255,0,0)$, $(0,255,0)$ and $(0,0,255)$ for these colors, respectively, whereas white and black are $(0,0,0)$ and $(255,255,255)$, respectively. Each of the remaining color possibilities are then defined by different channel combinations for R, G, and B and occur in the pink, yellow and turquoise regions.

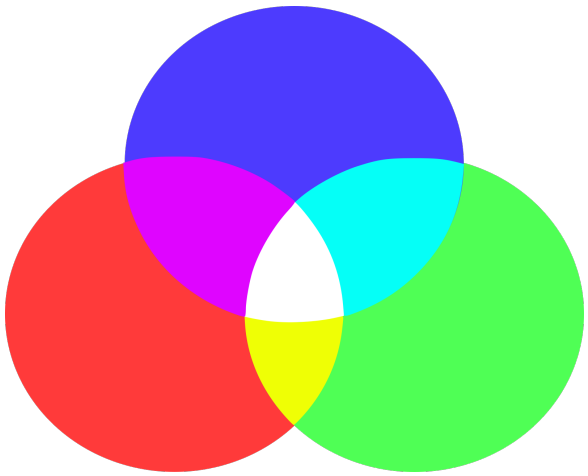

Figure 3.4: Simplified schematic describing how red, green blue mix to produce each of the $16,777,216$ possible color combinations in the RGB color model.

3.4 Reflectance Image Analysis

When working in the RGB color model, it is often useful and in some cases necessary to choose one specific color channel to work in. The simple reason for this is that every wavelength corresponds to a specific color and depending on the wavelength used, much and or even all detail contained in an image will not be visible. This is demonstrated in Fig 3.5, which shows a sample of single crystal Bi-2212 deposited onto a carbon tape substrate. In Fig 3.5(a), the original raw image taken by the reflectance microscope is shown. In this image much detail is visible, however it is somewhat dim and is likely due to the bandpass filter being far from its maximum intensity, resulting in a less intense image. Images in Fig 3.5(b) and Fig 3.5(d) correspond to the red and blue channels respectively. In both cases, they are completely dark and show no detail at all. Lastly, Fig 3.5(c) corresponds to the image in the green channel. This image is very sharp, with detail of the samples topography as well as a clear boundary between the sample and carbon tape substrate in the upper left hand corner.

3.4.1 Reflectance Rebinning Procedure

Using images obtained by reflection microscopy is a very useful tool in obtaining information on how radiation behaves at an interface. This method is by no means new, however a new binning procedure for analyzing reflectance images of both bulk and

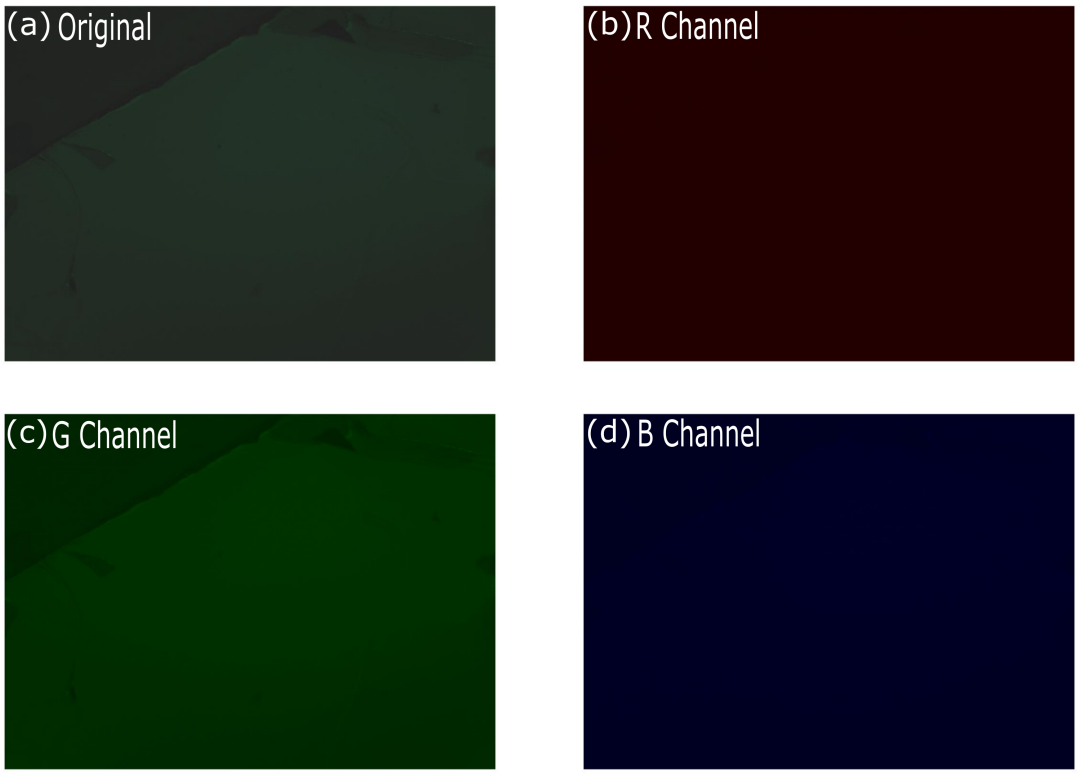

Figure 3.5: Single crystal Bi-2212 deposited on a piece of double sided carbon tape mounted to an aluminum SEM mount. (a) raw, original image obtained from reflectance microscopy at $\lambda = 532$ nm, (b) image in the blue channel, (c) image in the green channel, (d) image in the red channel.

thin layered samples deposited on substrates is presented below. Not only does this analysis provide a measure of reflection at a boundary, but also valuable information on the surface topography of the sample.

To begin, the sample image of interest such as that shown in Fig 3.6(a), is first imported into Python using the PIL package, where the image is scanned over to store both the position and corresponding G channel value for each pixel. Once this information is collected, the data is scanned through and the number of counts for each channel number is gathered and used to produce the distribution seen in Fig 3.6(b), which shows the distribution for the raw data collected over the full color channel range of $0 - 255$.

From the distribution shown in Fig 3.6(b), the G channel values are rebinned into bin sizes of three, meaning bin 0 now contains channels $0 - 2$, bin 1 contains channels

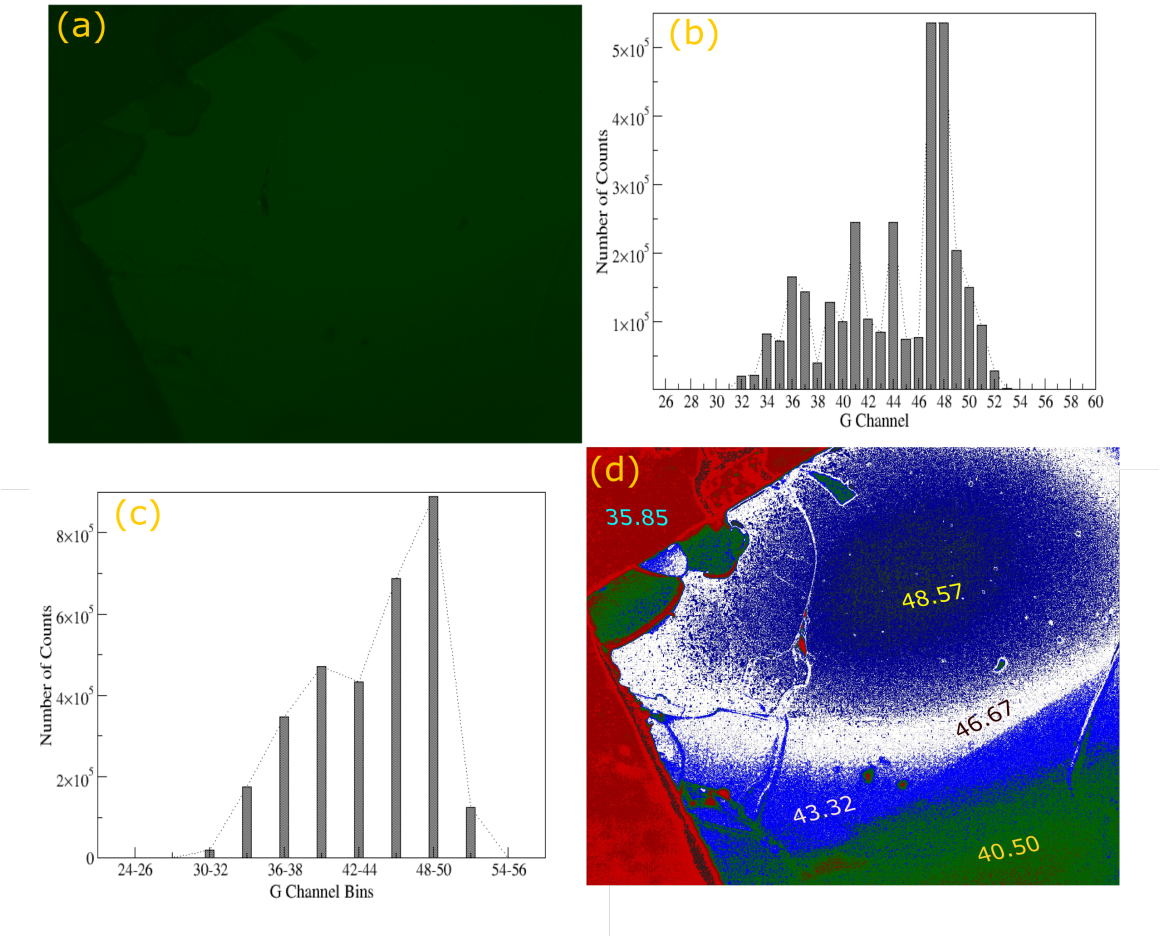

Figure 3.6: (a) Original raw image obtained via reflectance imaging where only the G channel values are used to construct the image. (b) Raw distribution indicating the number of counts in each G channel from image (a). (c) The distribution from (b) which has been partitioned to bin sizes of 3 to create sharply defined boundaries which will make layering and defects easier to see. (d) Relaying the rebinned data over the original image and defining each bin a its own color scale for sharp contrast between sample layers, substrates and topological defects.

$3-5$ and so on. By replotting the rebinned distribution of Fig 3.6(b), the result is that shown in Fig 3.6(c). By performing this rebinning procedure, it has allowed for the insertion of boundaries into an otherwise continuous distribution and with these channel boundaries defined, allows for one to identify the boundary between a sample and the underlying substrate, as well as areas of the sample with differing thicknesses. From here, the pixel positions corresponding to their respective channel

bins in Fig 3.6(c) were then assigned specific colors which are different from one another to allow for easier visual distinction for topographic and thickness information, with the resultant shown in Fig 3.6(d). In this image, the substrate was defined to be a dark red which sharply contrasts each of the colors representing areas of differing thickness across the sample. Furthermore, additional surface information was found to be visible when compared to the original G channel image (a). The red areas over the sample surface appeared to correspond to tape residue left over after exfoliating the sample. Moreover, this remaining tape residue also would account for the multiple shades of red seen over the substrate region.

3.5 Optical Constants of Bi-2212 Crystals via Reflectance Analysis

Using the collected reflectance images of Bi-2212, two separate methods were used to extract estimates of both the refractive index and extinction coefficient. First, Kramers-Kronig transformations were performed using extracted reflectance measurements from these images to obtain the first estimate and a slightly refined optical contrast method was used to obtain a second estimate. At the end of this section, optical constants are tabulated and compared to those presented in previously published literature.

Kramers-Kronig Results

In order to use the Kramer-Kronig relations, reflectance measurements were first performed on samples TC90, TC91 and TC78. After the rebinning procedure described in Chapter 4 was performed, the images in Fig 3.7 were obtained. For Fig 3.7(a), a highly reflective broadband dielectric mirror (item number BB0511-E02) was placed under the objective to measure the reflected light intensity since this provides an accurate measure of the incident light intensity. From the image, the Gaussian distribution of the beam is visible, and 171.90 was used as the maximum intensity of the incident beam.

Fig 3.7(b)-(d) correspond to samples TC90, TC91 and TC78 respectively. TC90 had a relatively clean surface with clear distinction seen between the boundaries and

only minute surface contamination, while TC91 was seen to have a pristine surface with two different layers visible and no surface defects. In the case of TC78, two different layers were visible, however the surface was highly erratic, with multiple cracks and divots present. Taking the ratio between the intensity of the reflected light and the largest measured intensity for each sample, the reflectances of each sample were found to be

$$R_{T90} = \frac{I_{90K}}{I_{mirror}} = 0.270,$$

$$R_{T91} = \frac{I_{91K}}{I_{mirror}} = 0.252, \tag{3.15}$$

$$R_{T78} = \frac{I_{90K}}{I_{mirror}} = 0.270.$$

With the reflectance known, Eqn 3.8 was then used to obtain the phase dependence on both n and κ, which is shown in Fig 3.8. With such a large phase dependence on both optical constants, the correct phase corresponding to the wavelength used in this work ($\lambda = 532$ nm) was calculated using Eqn 3.9. With no information on the reflection function $R(\omega')$ in Eqn 3.9, it was constructed based on the full reflectance spectrum collected previously [1]. The spectrum collected was characterized by three distinct features, which are shown in Fig 3.9.

First, there is a sharp drop from 100% reflectance to a minimum over the range $0 \sim 10,400$ cm^{-1}. The function then slowly increases to $\sim 25,000$ cm^{-1}, where a small step occurs in the function where the reflectance remains relatively constant for all frequencies beyond this point. Since each feature is a line segment, the equations of each section are

$$\begin{aligned} R_1(\omega') &= -7.58 \times 10^{-5}x + 0.915 \quad x < A, \\ R_2(\omega') &= 1.87 \times 10^{-6}x + 0.0585 \quad A < x < B, \\ R_3(\omega') &= 4.34 \times 10^{-7}x + 0.184 \quad x > B. \end{aligned} \tag{3.16}$$

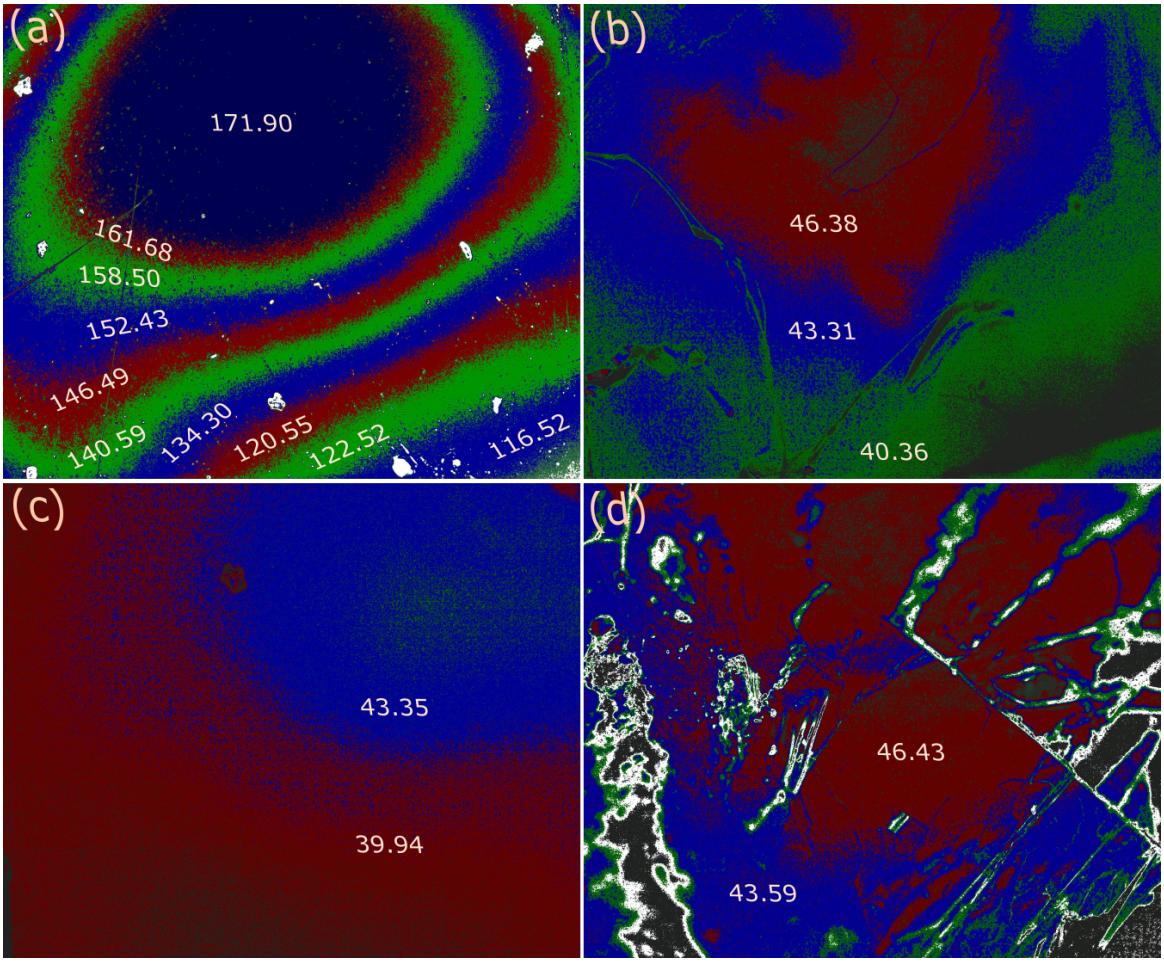

Figure 3.7: Rebinned reflectance images showing (a) the intensity of the incident light and samples (b) TC90 (c) TC91 and (d) TC78.

From here, the following transformation on Eqn 3.9 was performed,

$$\Theta(\omega) = \frac{\omega}{\pi}\int_0^\infty \frac{\ln R(\omega') - \ln R(\omega)}{\omega^2 - \omega'^2}\mathrm{d}\omega' \Rightarrow \frac{\omega}{\pi}\sum_0^{\omega'_c} \frac{\ln R(\omega') - \ln R(\omega)}{\omega^2 - \omega'^2}\Delta\omega', \qquad (3.17)$$

where the cutoff frequency ω'_c was chosen to be an arbitrarily large value (1.2×10^6 cm^{-1}) such that $\omega'_c >> \omega'$ to allow for convergence. By using the boundary conditions for $R(\omega')$ shown in Eqn 3.16, Fig 3.10 was obtained, where convergence was found to occur near 30,000 cm^{-1}. Moreover, the two distinct features at $10,000$ cm^{-1} and 25,000 cm^{-1} correspond to the changes in slope seen in Fig 3.9, further indicating $\Theta(\omega)$ follows the reflectance function $R(\omega')$ from Fig 3.10.

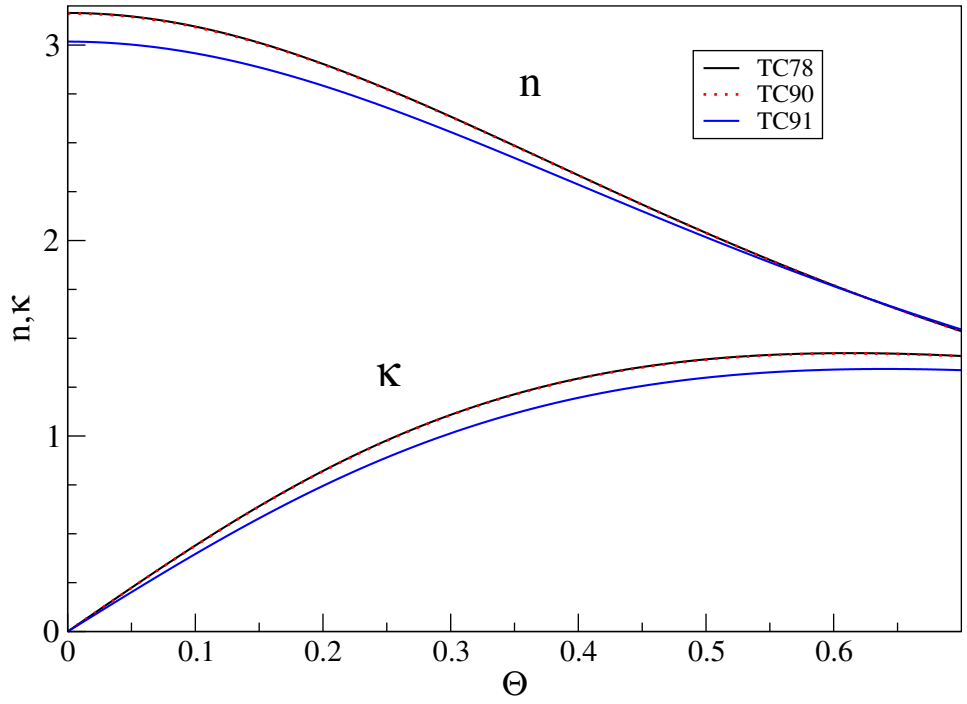

Figure 3.8: Refractive index and extinction coefficient curves calculated using Eqn 3.8. Curves corresponding to TC78 and TC90 were found to nearly overlap.

For a wavelength of 532 nm ($18,800\ \mathrm{cm}^{-1}$), Θ was found to be 0.0356. This appears to be a reliable estimate since $R(\omega')$ showed relatively small change in reflectance past boundary point A. Using the phase, n and κ were extracted from each of the three curves from Fig 3.8, yielding for each sample

$$\begin{aligned} \tilde{n}_{TC78} &= 3.16 + 0.160i, \\ \tilde{n}_{TC91} &= 3.01 + 0.144i, \\ \tilde{n}_{TC90} &= 3.15 + 0.160i. \end{aligned} \tag{3.18}$$

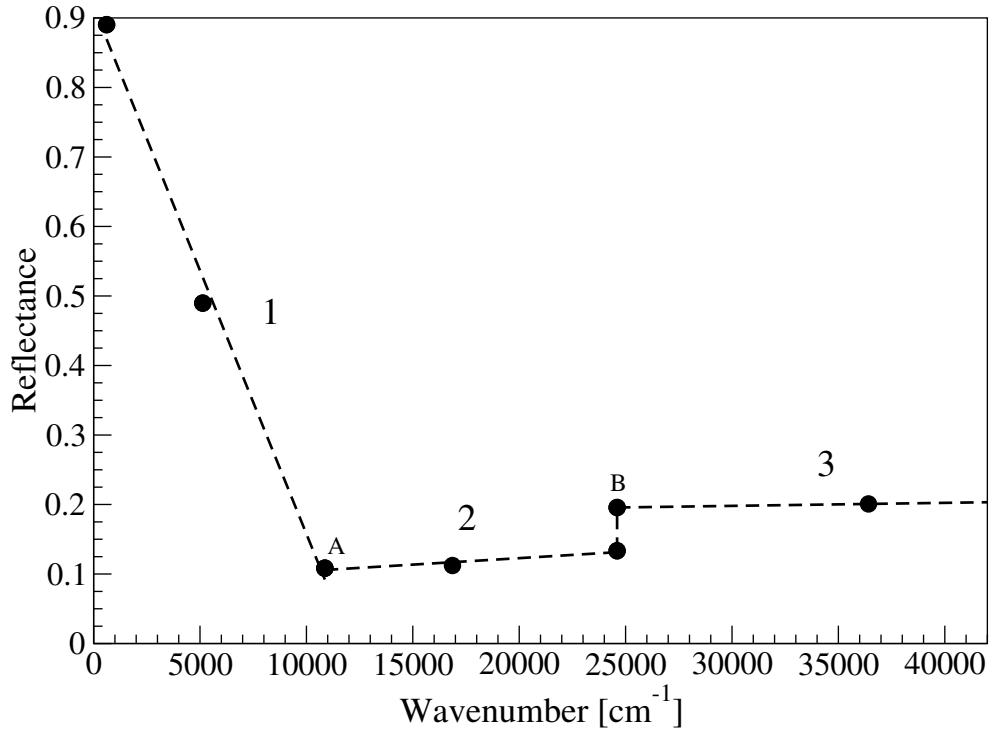

Figure 3.9: Reflectance function $R(\omega')$ built from a collected reflectance spectrum presented in the literature [1]. Multiple data points were extracted from the provided reflectance spectrum and a linear fit each of the three main features labelled 1, 2 and 3 was performed, with their respective equations shown in Eqn 3.16.

Optical Contrast

As a preliminary test for the modified optical contrast method, TC91 was attached to carbon tape which was then attached to an aluminum SEM mount, where the tape plays the role of the oxide layer and the aluminum mount serves the purpose of the underlying substrate (refer to Fig 3.1). Using SEM, the thickness of both the sample and carbon tape was found to be 8.78 μm and 51.79 μm, respectively, as shown in Fig 3.11. Here it is noted that from the figure, the sample was not normal to the electron beam and the thicknesses shown were likely an overestimation.

With the complex refractive indices of both carbon and aluminum being $\tilde{n} = 2.43 + 0i$ and $\tilde{n} = 0.939 + 6.42i$, respectively [30, 33], the only unknown parameters

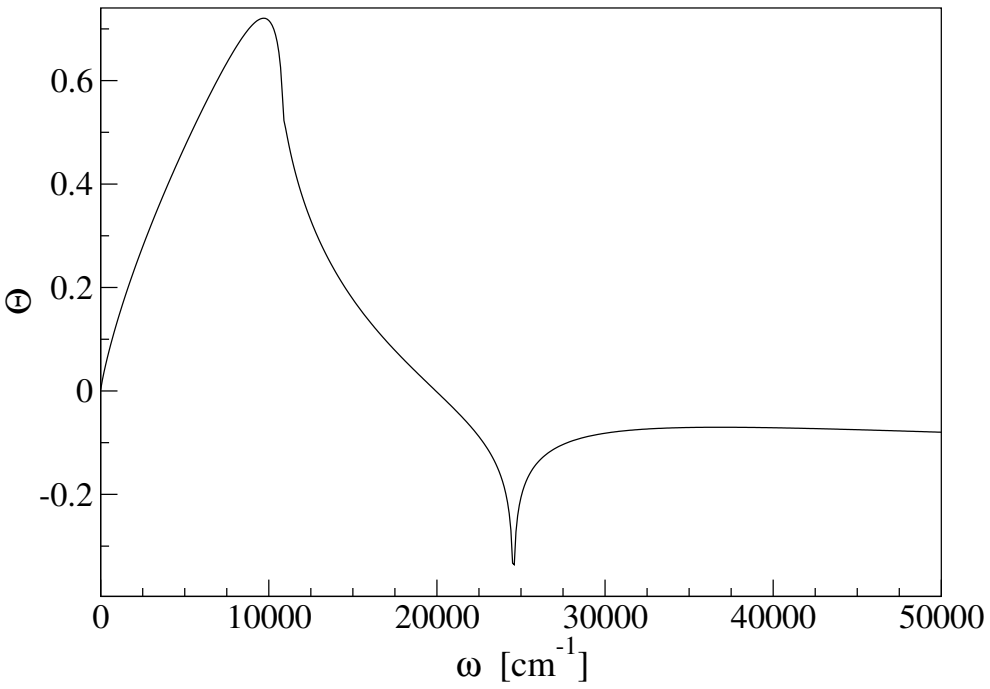

Figure 3.10: Calculated phase curve using Eqn 3.9, with the cutoff of $\omega_c = 1.2 \times 10^6$ cm^{-1} to achieve convergence.

in Eqns 3.1-3.2 were the refractive index and extinction coefficient of Bi-2212. Being the same sample as shown in Fig 3.6, OC was calculated using Eqn 3.12 to be 0.355 by using the reflectance values of the substrate as well as the thickest portion of the sample, 35.85 and 48.57, respectively. Using Eqns 3.1-3.2, selections of n and κ were then chosen where like solutions of OC obtained via reflectance imaging were searched for. Beginning with $n = 1.00$, κ was iterated through with values $0.0001 - 10$ with a stepsize of 1×10^{-5}. Once completed, n was increased by 0.01 and the procedure was repeated until $n = 7.00$.

Initially, multiple solutions arose but as the tolerance was tightened to 0.01%, only one solution was found to agree, which was when $\tilde{n} = 6.43 + 0.003i$. With n being extremely large and conversely κ very small, both solutions were found to be unlikely. The most probable cause of error in this method was the sample setup itself. With a penetration depth of ~ 60 nm at the working wavelength of 532 nm [1], there was little to no transmission once light entered the sample, since its thickness is 8.7

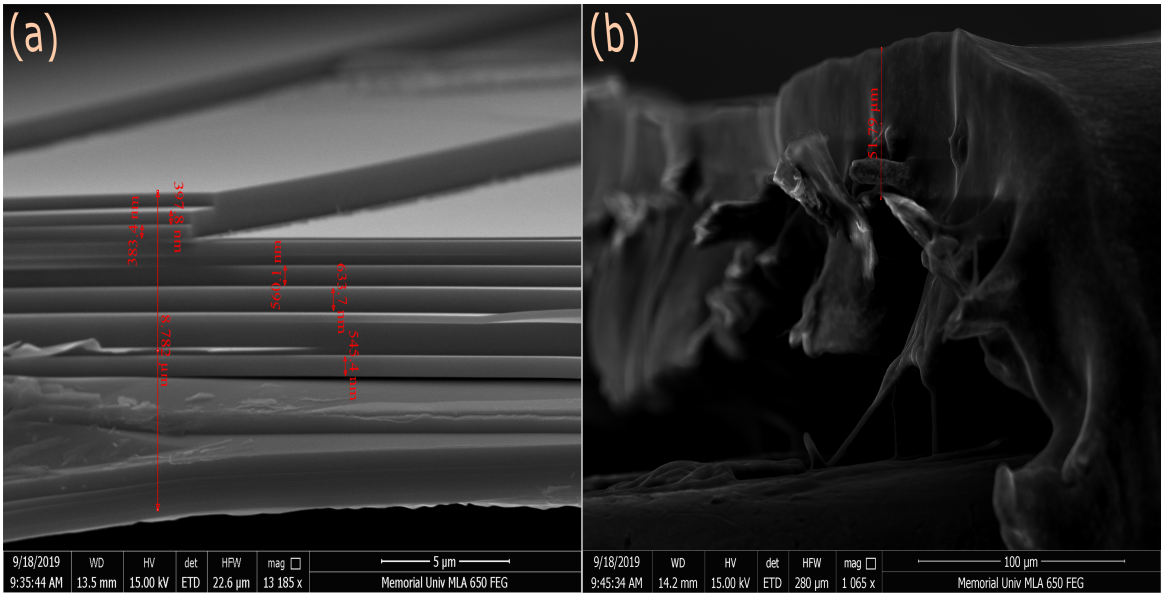

Figure 3.11: SEM images used to determining thicknesses of (a) TC91 and (b) underlying carbon tape. From (a), the measured thicknesses appear to be overestimates since the measurements did not occur at normal incidence.

μm. Moreover, any light which had been transmitted through the sample likely was not penetrating the underlying carbon tape to the alumnium mount below as it was opaque and also very thick. It was likely that the overestimate of the thickness of TC91 from SEM measurements also had an impact on the resulting refractive index and extinction coefficient. This was briefly investigated, where the thickness was decreased by 15% and resulted in $\tilde{n} = 5.08 + 007i$.

In order to test the method properly, an adequate substrate with an oxide layer is needed with a sample that is < 60 nm thick. For reason, the optical constants obtained by optical contrast were not used in any remaining calculations in this thesis.

3.5.1 Results & Discussion

Table 3.1 presents the optical properties determined by reflectance and Kramers-Kronig analysis in this work, along with those determined previously in the visible light region. Firstly, it was noted that the measured reflectances for samples TC78, TC90, and TC91 were close to one another, with the same reflectance measured for both TC78 and TC90. Reflectance is both surface and thickness dependent, and with TC78 samples not planar, this likely impacted measurements on this particular

Table 3.1: Optical properties of Bi-2212 obtained from this work and previously published literature for studies which were performed in the visible near-infrared region. a, b, c subscripts correspond to measurements along the respective crystallographic axes.

	T_c [K]	λ [nm]	R	n	κ	ϵ_1	ϵ_2	Re(σ) [Ωcm^{-1}]
Reflectance + KK (Present Work)	78	532	0.270	3.2±0.6	0.160±0.03	9.6±4	1.0±0.4	-
	90		0.270	3.2±0.6	0.160±0.03	9.9±4	1.0±0.4	-
	91		0.252	3.0±0.6	0.144±0.03	9.0±4	0.9±0.4	-
Reflectance + KK [21]	86	532	0.106^a	-	-	3.48^a	-	364
			0.123^b	-	-	4.14^b	-	364
Reflectance + KK [1]	-	532	0.118	-	-	3.48	1.72	563
HAUP [13]	90	488	-	1.89^a	0.43^a	3.40^a	1.64^a	560^a
				2.04^b	0.39^b	4.01^b	1.58^b	540^b
				2.09^c	0.29^c	4.27^c	1.23^c	420^c
Reflectance + KK [19]	90	855	-	5.80	-	-	-	-

sample.

Using the determined refractive index and extinction coefficient for each sample, the real and imaginary dielectric constants were calculated using Eqn 3.10. It was noted that the associated uncertainties were relatively high for both n and κ ($\sim 20\%$), which is based on several experimental factors. Firstly, as shown in Chapter 2, it was found that both TC90 and TC91 have $\sim 5\%$ deviation in thickness over the length of each sample, meaning there was not completely normal incidence. Secondly, the error associated with the collected RGB values for each pixel by the camera and software must be considered as well as the quality of each samples surface.

From Table 3.1, the refractive index was found to increase with increasing wavelength, a promising observation since n is typically found to depend on λ monotonically over such a small spectral range. Comparing ϵ_2 values at 532 nm, results in this work were found to be approximately three times larger than those obtained previously [1, 21]. Both sample quality and thickness impact the measured reflectance of Bi-2212 and this was likely the cause of these discrepancies as well as the measured

reflectance in this work being almost twice that of previous measurements at this wavelength.

Chapter 4

Brillouin Light Scattering on Bi-2212

4.1 Theory

4.1.1 Phonons

To gain a full understanding of phonons and phonon behavior, one may first recall a simple harmonic oscillating system. In quantum mechanics, a harmonic oscillator will have energy

$$E_m = \hbar\omega(m + \frac{1}{2}), \tag{4.1}$$

where ω is the angular frequency and m is the excitation state describing the vibration of atoms in the lattice [39]. These vibrational states are defined as phonons and describe the elastic behavior of atoms in the crystal lattice. Of these vibrational states, each corresponds to a normal mode [39]. These modes can be explained using the classical picture seen in Fig 4.1, where a chain of two distinguishable atoms of masses M_1 and M_2 are aligned periodically one after the other and are attached by springs with a spring constant K. By considering only nearest neighbor interactions, Newtons second law may be written as

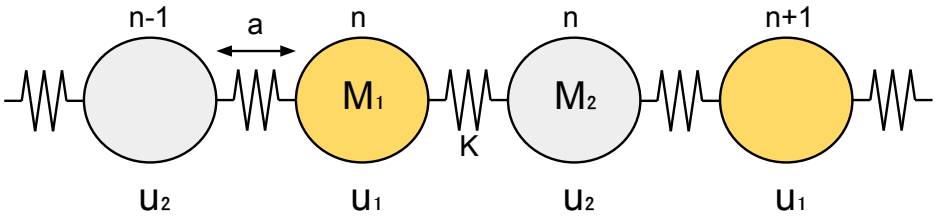

Figure 4.1: Linear diatomic chain of two distinguishable atoms with mass M_1 and M_2 respectively. Each mass is attached by a spring of length a with a uniform spring constant K.

$$\begin{aligned} M_1\ddot{u_1} &= K(u_2^n - u_1^n) + K(u_n^{n-1} - u_1^n), \\ M_2\ddot{u_2} &= K(u_n^{n+1} - u_2^n) + K(u_1^n - u_2^n), \end{aligned} \tag{4.2}$$

where each atom oscillates about the equilibrium position n. A plane wave solution is assumed, given by

$$u_i = C_i e^{ikna - i\omega t}, \tag{4.3}$$

where k is the wavenumber, ω is the angular frequency, t is time, and C_i is an arbitrary constant associated with vibration of the i^{th} atom. By substituting Eqn 4.3 into Eqn 4.2 and taking the derivative of the left hand side, one obtains

$$\begin{aligned} -M_1\omega^2 C_1 &= K(-2C_1 + C_2 + C_2 e^{-ika}), \\ -M_2\omega^2 C_2 &= K(-2C_2 + C_1 e^{ika} + C_1). \end{aligned} \tag{4.4}$$

From here, a non-trivial solution emerges only when the determinant is zero [18], yielding

$$\begin{bmatrix} -M_1\omega^2 + 2K & -K(1+e^{-ika}) \\ -K(1+e^{ika}) & -M_2\omega^2 + 2K \end{bmatrix} \begin{bmatrix} C_1 \\ C_2 \end{bmatrix} = 0. \tag{4.5}$$

Solving for ω yields [25]

$$\omega(k) = \sqrt{K}\left(\frac{(M_1+M_2) \pm \sqrt{M_1^2 + M_2^2 + 2M_1M_2\cos(ka)}}{M_1M_2} \right)^{\frac{1}{2}}, \tag{4.6}$$

which has small k solutions given by [25]

$$\begin{aligned} \omega(k) &= \sqrt{\frac{2K(M_1+M_2)}{M_1M_2}} \equiv \omega_o(k), \\ \omega(k) &= ka\sqrt{\frac{K}{2(M_1+M_2)}} \equiv \omega_a(k). \end{aligned} \tag{4.7}$$

These two solutions correspond to the optical and acoustic phonon branches which are shown in the phonon dispersion curve in Fig 4.2. Optical phonons corresponds to high energy excitations which occur from atoms in the unit cell vibrating out of phase with respect to one another while acoustic phonons are low energy and exist due to displacements of atoms vibrating in phase in the unit cell [25].

By extension of the above example, considering the same system of n atoms in three dimensions yields $3n$ modes [18]. Of this total number, $3n-3$ modes correspond to optical phonons and the remaining 3 modes correspond to acoustic modes [18]. For a typical crystalline material, the set of acoustic modes are comprised of two quasi-transverse modes and one quasi-longitudinal mode.

4.1.2 Brillouin Light Scattering

Brillouin scattering is a form of inelastic light scattering used to investigate thermally excited acoustic phonons. When a photon is incident on a material, both energy and

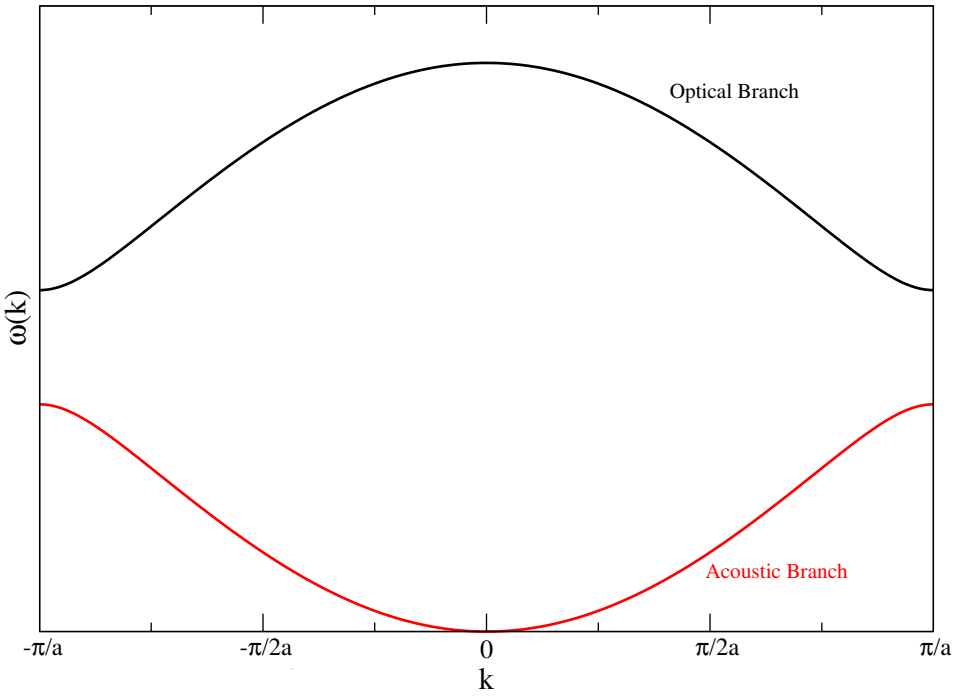

Figure 4.2: Dispersion curve for the optical and acoustic phonons branches confined to the first Brillouin zone from Eqn 4.7.

momentum are conserved and are described by

$$\begin{aligned} \hbar\omega_s &= \hbar\omega_i \pm \hbar\Omega, \\ \hbar\mathbf{k}_i &= \hbar\mathbf{k}_s \pm \hbar\mathbf{q}, \end{aligned} \tag{4.8}$$

where $\omega_{i,s}$ are the angular frequencies of the incident and scattered photon, respectively, Ω is the angular frequency of the phonon in the material, $\mathbf{q}$ is the wavevector of the phonon in the material and $\mathbf{k}_{i,s}$ are the incident and scattered wavevectors of the photon, respectively. Moreover, the angular frequency is given by

$$\Omega = 2\pi f = vq, \tag{4.9}$$

where f and v are the phonon frequency and velocity of the phonon, respectively. Since $v << c$, where c is the speed of light, it is assumed that $|\mathbf{k}_i| \approx |\mathbf{k}_s|$.

From the conservation laws described in Eqn 4.8, a phonon will be either created or annihilated in the bulk when a photon is incident on a material. When a phonon is created, the scattered photon energy will be less than that of the incident photon and conversely when a phonon is annihilated, the scattered photon energy will be greater. These two processes are referred to as Stokes and Anti-Stokes scattering, respectively.

The interaction of photons with thermal phonons gives rise to surface ripple effects or the elasto-optic mechanism. These are seen by phonons which propagate either along the surface of the material or through the bulk, respectively, where a schematic of both processes is shown in Fig 4.3. Referring to the diagram, the surrounding medium is typically air or vaccuum which has a refractive index of 1. For this reason, the refractive index of the sample medium is simply labelled n.

For phonons propagating through the bulk, q has both parallel and perpendicular components where the magnitude of each is, respectively

$$\begin{aligned} q_B^{\parallel} &= nk_i \sin\theta_i' + nk_s \sin\theta_s', \\ q_B^{\perp} &= nk_i \cos\theta_i' + nk_s \cos\theta_s', \end{aligned} \tag{4.10}$$

where θ_i' and θ_s' are the refracted internal angles corresponding to the incident and scattering angles, respectively. The magnitude of q_B is written as

$$q_B = \sqrt{(nk_i \sin\theta_i' + nk_s \sin\theta_s')^2 + (nk_i \cos\theta_i' + nk_s \cos\theta_s')^2}. \tag{4.11}$$

By expanding out Eqn 4.11 and recalling $k_i \approx k_s$, one obtains

$$q_B = nk_i\sqrt{2 + 2(\sin\theta_i' \sin\theta_i + \cos\theta_i' \cos\theta_i)}. \tag{4.12}$$

Using the indentity $\sin\theta_i' \sin\theta_i + \cos\theta_i' \cos\theta_i = \cos(\theta_i' - \theta_s')$ and the conservation of energy in Eqn 4.8, Eqn 4.12 is reduced to

$$2\pi(\omega_s - \omega_i) = f_B = \frac{v_B n}{\lambda_i}\sqrt{2[1 + \cos(\theta_i' - \theta_s')]}. \tag{4.13}$$

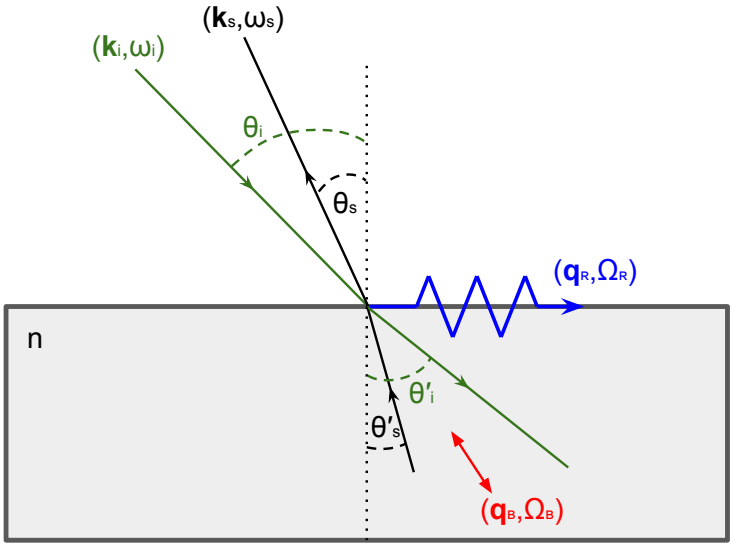

Figure 4.3: Schematic of the processes which occur when thermally excited phonons are probed via Brillouin light scattering. Vectors **k** and **q** are the incident photon and phonon wavevectors respectively, Ω is the angular frequency of a phonon, $\theta(\theta')$ is the external(internal) angle and n is the refractive index. Furthermore i, s correspond to incident and scattering and R, B refer to Rayleigh surface and bulk.

Lastly, by using the double angle identity $\sin\frac{\theta}{2} = \pm\sqrt{\frac{1-\cos\theta}{2}}$, Eqn 4.13 becomes

$$f_B = \frac{2v_B n}{\lambda_i}\sin\left(\frac{\theta}{2}\right), \tag{4.14}$$

where $\theta = \pi - \theta_i' + \theta_s'$. For 180° backscattering, $\theta = 180°$ which reduces $\sin\frac{\theta}{2}$ to 1 and the bulk phonon velocity becomes

$$v_B = \frac{f_B\lambda_i}{2n}. \tag{4.15}$$

Phonons which propagate along the surface are called Rayleigh surface modes. Surface phonon amplitude decreases exponentially with depth [34], resulting in the vector **q** having only a parallel component, with its magnitude equal to

$$q_R = k_i\sin\theta_i + k_s\sin\theta_s, \tag{4.16}$$

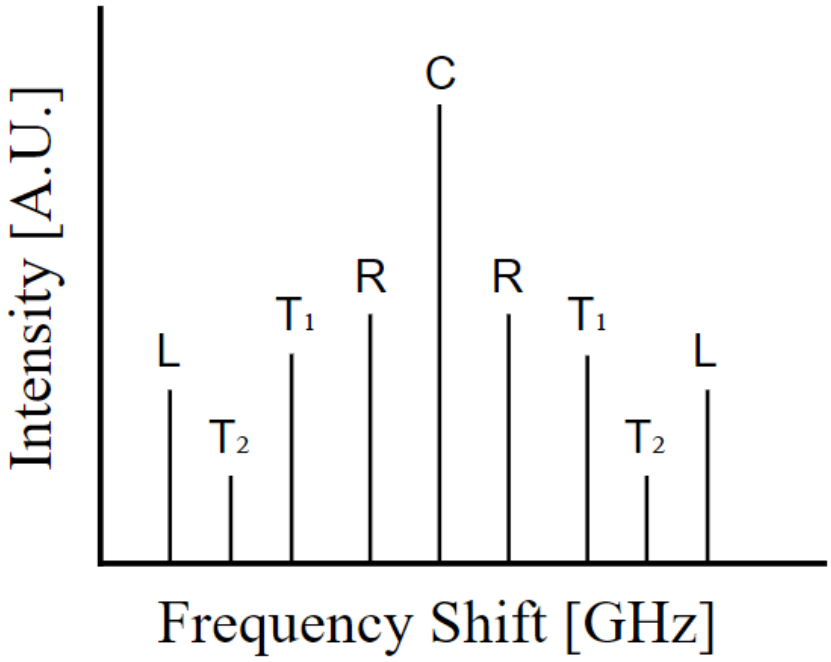

Figure 4.4: Schematic of a typical Brillouin spectrum for an opaque, crystalline material. C is the elastic central line assigned a frequency shift of 0 GHz, with the Rayleigh surface mode R, quasi-transverse bulk modes $T_{1,2}$ and quasi-longiduinal bulk mode L symmetric on either side. Peaks to the left and right of the central line correspond to Stokes and Anti-Stokes scattering processes, respectively.

where θ_i and θ_s correspond to the external incident and scattering angles, respectively. In the case of 180° backscattering geometry, $\mathbf{k}_i$ is antiparallel to $\mathbf{k}_s$, resulting in $\theta_i = \theta_s$. Using this and the fact that $k_i \approx k_s$, Eqn 4.16 becomes

$$q_R = 2k_i \sin\theta_i. \tag{4.17}$$

Using Eqn 4.9 and $k_i = 2\pi/\lambda_i$, the Rayleigh phonon velocity is given by

$$v_R = \frac{f_R \lambda_i}{2\sin\theta_i}, \tag{4.18}$$

where λ_i is the wavelength of the incident photon.

Fig 4.4, presents an example of a typical Brillouin spectrum expected from an opaque material. The left and right sides of the elastic central line (C) are the Stokes and Anti-Stokes peaks due to the quasi-longitudinal bulk (L), quasi-transverse bulk

(T_1, T_2) and Rayleigh surface (R) modes, respectively. The central line is assigned a frequency shift of 0 GHz and the frequency shift of each Brillouin peak is measured with respect to it. The Rayleigh surface mode has the smallest frequency shift, which is typically measured between 0 and a few tens of GHz from the central line. The bulk transverse and longitudinal peaks occur outside of this range and can appear as far as a few hundred GHz from the central line. With such small frequency shifts, a tandem Fabry-Perot interferometer is used to make observing these modes possible.

A collected spectrum will consist of peaks corresponding to frequencies of phonon modes which have a full width at half maximum ($FWHM$) defined as [37]

$$FWHM = \frac{2f_0\kappa}{n}, \tag{4.19}$$

where f_0 is the frequency shift and is equal to

$$f_0 = 2nkv, \tag{4.20}$$

with v being the acoustic phonon velocity.

4.2 Optical System

Fig 4.5 shows the Brillouin light scattering setup with backscattering geometry used in this work. A Nd:YVO_4 laser was the light source used, with a wavelength of 532 nm and an output power of 1.77 W. The beam first passes through the variable neutral density filter V_1 to be attenuated before passing through the half-wave plate (HWP) which changes vertically polarized light to horizontally polarized. From here, the beam reaches a beam splitter (BS) where a portion of the beam is reflected and the remaining light is transmitted. The reflected portion passes through the aperture A, where it is the reflected by mirror M_2, attenuated further by variable neutral density filter V_3 and acts as a reference beam for the tandem Fabry-Perot interferometer (FPI).

The transmitted portion of the beam reaches mirror M_1 where it is reflected by 90° and passes through two filters F_1 and F_2 before before further attenuation by variable neutral density filter V_2, where the beam has a power of 10 mW. Once attenuated, the beam reaches the prism P where it is reflected by 90° and passes through camera

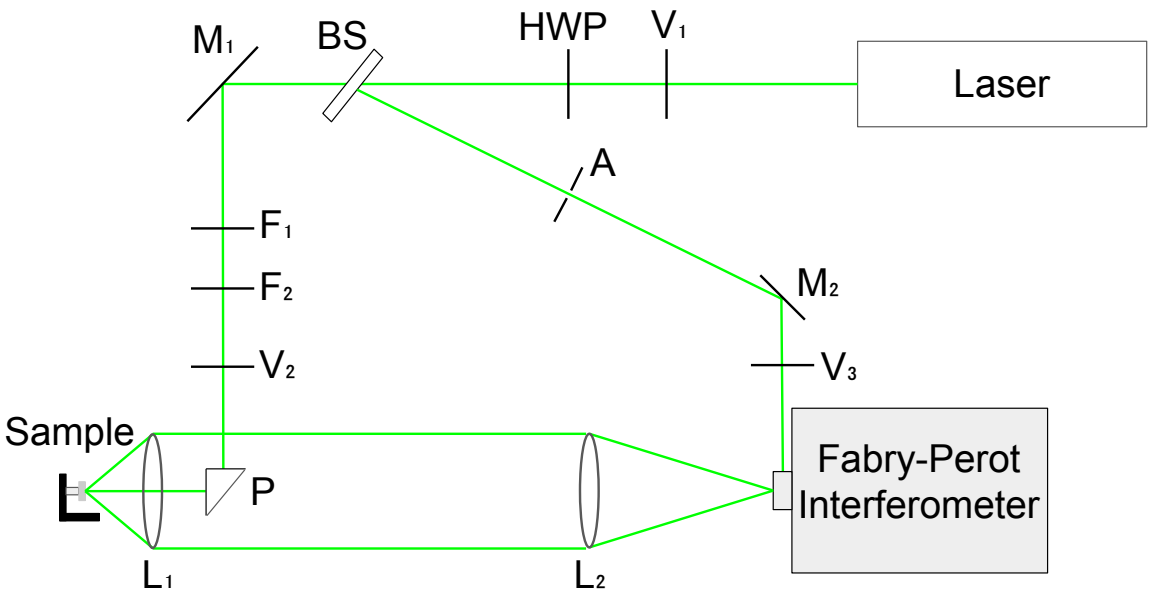

Figure 4.5: Brillouin light scattering setup used where V - variable neutral density filter, HWP - half-wave plate, BS - beam splitter, M - mirror, F - filter, P - prism and L - lens.

lens L_1, which has a focal length of 5 cm and an aperture of f/2.8. The beam then strikes the sample mounted to a sample stage which rotates, allowing for the incident angle to be set between $0° - 80°$. Light scattered from the sample is collected and collimated by L_1. The collimated beam then passes through the focusing lens L_2 with a focal length of 40 cm and is focused onto the pin hole entrance of the FPI. The pinhole size was either 300 μm or 450 μm, the former used when the central elastic peak width needed to be reduced to reveal Brillouin peaks at very small frequency shifts.

The interferometer used in this work is a six-pass tandem Fabry-Perot interferometer produced by JRS instruments. This interferometer is constructed of two Fabry-Perot interferometers as shown Fig 4.6 each of which consists of two extremely flat and reflective mirrors separated by a distance d_i where $i = 1, 2$. For a wavelength to successfully transmit through a given Fabry-Perot interferometer, it must satisfy [32]

$$d_i = \frac{m\lambda}{2}, \tag{4.21}$$

where m is an any integer.

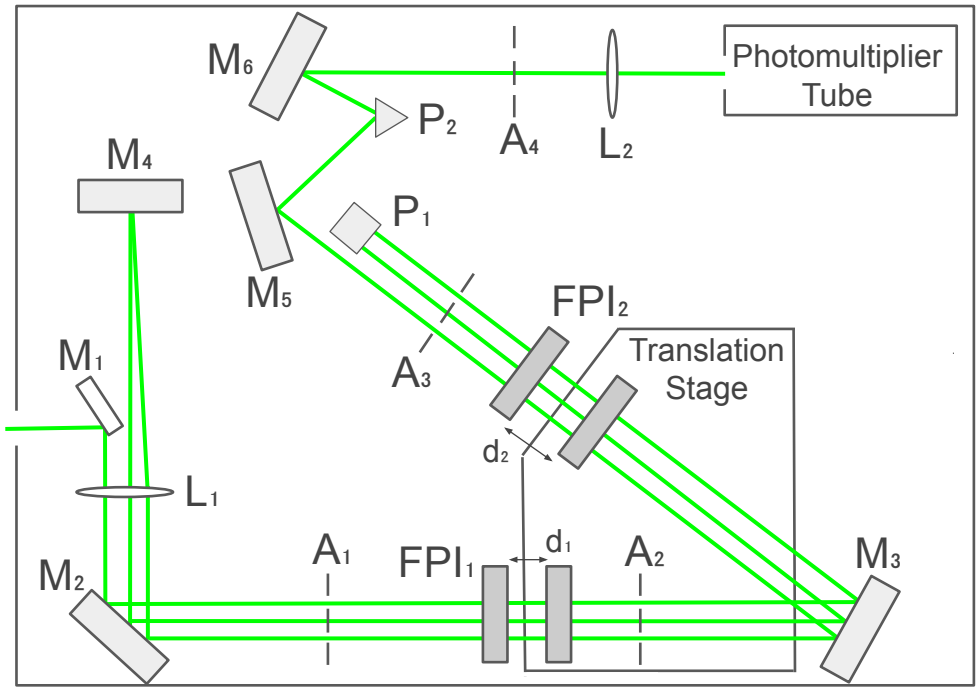

Figure 4.6: Optical setup for a six pass tandem Fabry-Perot interferometer, where M - mirror, L - lens, A - aperture, FPI - Fabry-Perot interferometer, d - spacing of Fabry-Perot interferometer and P - prism.

Once scattered light from the sample is collimated and passes through the pinhole entrance in the Fabry-Perot interferometer, it is reflected 90° twice by mirrors M_1 and M_2, where it then passes through aperture A_1 and reaches the first Fabry-Perot interferometer (FPI_1) at normal incidence. At this point, the wavelengths which transmit through are only those with frequencies satisfying the conditional statement [32]

$$f_m = \frac{mc}{2d_i}. \tag{4.22}$$

Light corresponding to these frequencies then passes through aperture A_2 and are reflected by mirror M_3 to the second Fabry-Perot interferometer (FPI_2) where as before, light only with frequencies satisfying Eqn 4.22 passes through. Light passing through FPI_2 passes through aperture A_3 and strikes the prism P_1, where it is back reflected and again passes through both FPI_2 and FPI_1 as well as apertures A_3, A_2 and A_1. Light reaches mirror M_2 for a second time, where it is reflected 90° back through lens L_1 and reaches mirror M_4 where at this point, the light is reflected back through lens L_1 and the same process of passing through both FPI_1 and FPI_2 is repeated

again. Once passing through FPI_2 for a third time, the light enters aperture A_3 and is reflected several times by mirror M_5, prism P_2 and mirror M_6. At this stage, the light passes through aperture A_4 and lens L_2, which focuses the light onto the output pinhole of the FPI and is then incident on a photomultiplier tube. This information collected by the photomultiplier tube is converted to an electronic signal and is passed to a computer which displays this information in the form of a spectrum showing the intensity as a function of frequency.

The resolution of a tandem Fabry-Perot interferometer is controlled by adjusting the separation spacing between each internal interferometer inside of the unit. This spacing defines the free spectral range (FSR), which is the difference between two consecutive maximum transmission frequencies [32, 40]

$$FSR = \nu_{m+1} - \nu_m = \frac{c}{2d_i}, \tag{4.23}$$

where ν_i is the transmission frequency, c is the speed of light, and d_i is the mirror spacing, where $i = 1, 2$.

Using the full width of the elastic peak, $\mathcal{E}$, and FSR, the finesse is given by [32]

$$F = \frac{FSR}{\mathcal{E}}, \tag{4.24}$$

which gives the resolution of the tandem Fabry-Perot interferometer [40]. Finesse is highly influenced by the quality of mirrors used in each Fabry-Perot interferometer. The reflectivity and surface of the mirrors play a key role in achieving a high finesse as a low reflectance or surface defects on these mirrors results in a loss of signal.

In the setup just described, light entering the tandem Fabry-Perot interferometer makes three passes through both Fabry-Perot interferometers, yielding a total of six passes. With each pass, light is being further filtered allowing for a drastic increase in contrast. This high contrast is necessary when probing acoustic phonons in Brillouin light scattering experiments as signals measured are extremely weak.

4.3 Results & Discussion

4.3.1 Brillouin Spectra

Figs 4.7−4.12 present the Brillouin spectra collected on samples TC78 and TC91. Each set of spectra was collected with θ_i ranging between $10° - 75°$ from the samples normal. In these spectra, six different modes were observed with corresponding frequency shifts shown in Table 4.1 obtained via Lorentizian fitting. By comparing observed acoustic modes with those from previous Brillouin studies [22], the smallest shift is found to be the Rayleigh surface mode while the next two consecutive modes are the two quasi-transverse bulk modes, each denoted as R, T_1 and T_2, respectively. The observed quasi-longitudinal bulk mode is labeled as L which was determined based on its characteristic broad shape and low intensity. The remaining two modes were unknown and labeled as U_1 and U_2, respectively.

4.3.1.1 TC78-1

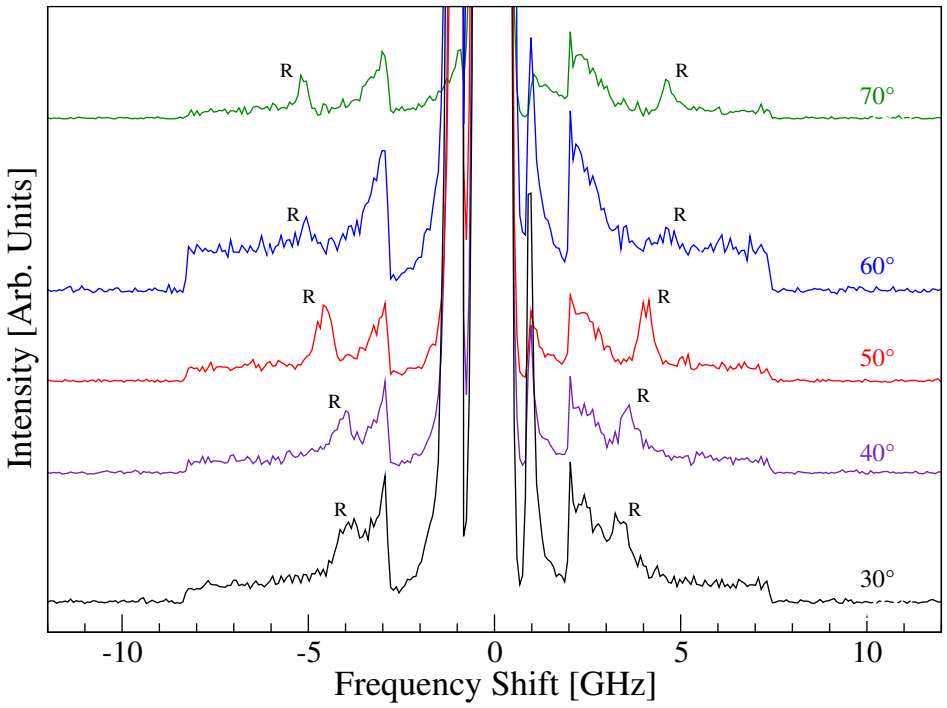

Figure 4.7: Raw Brillouin spectra of TC78 at room temperature with an FSR of 30 GHz. R corresponds to the Rayleigh surface mode.

Fig 4.7 presents Brillouin spectra of sample TC78 collected with θ_i ranging from $30° - 70°$. Spectra were collected using the segmentation window which is a feature used to spend 10 times longer scanning over a specific frequency range. Referring to the figure, spectra were collected with the segmentation window ranging from approximately $2 - 7.5$ GHz.

4.3.1.2 TC78-2

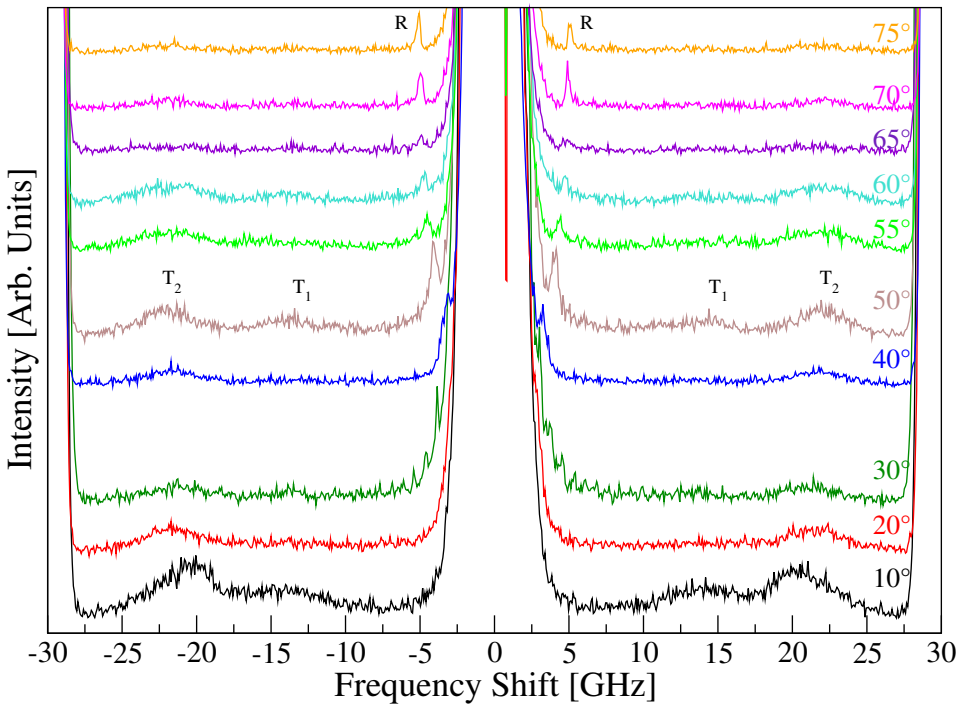

Figure 4.8: Raw Brillouin spectra of TC78 at room temperature with an FSR of 30 GHz. R, T_1 and T_2 correspond to the Rayleigh surface mode and two quasi-transverse modes, respectively.

Fig 4.8 presents the spectra of sample TC78 collected with θ_i ranging from $10° - 75°$. The Rayleigh surface mode was observed for $\theta_i > 40°$. Two quasi-transverse modes were observed over the entire angular range probed and were found to have no angular dependence.

4.3.1.3 TC91-1

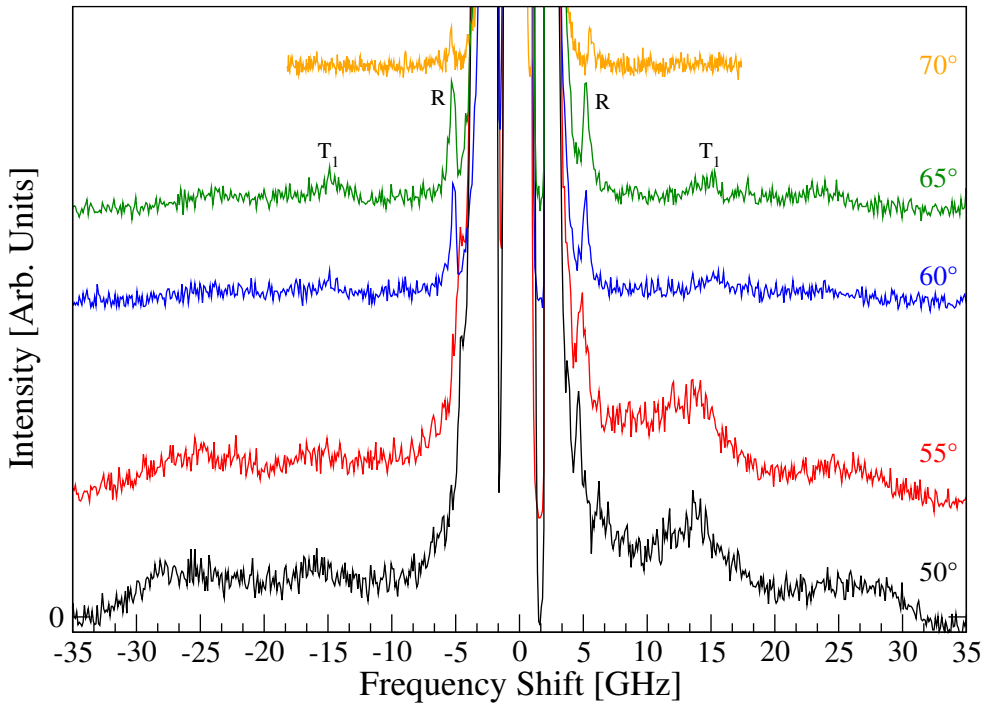

Figure 4.9: Raw Brillouin spectra of TC91 collected at room temperature. R and T_1 correspond to the Rayleigh and quasi-transverse modes, respectively.

Fig 4.9 presents the spectra of sample T91 collected with θ_i ranging from $50° - 70°$ with an FSR of 30 GHz for spectra collected with $\theta_i < 70°$ and an FSR of 20 GHz for $\theta_i = 70°$. The Rayleigh surface and first quasi-transverse modes were again observed, however compared to spectra collected on sample TC78, the quality of TC91 spectra is much lower. Moreover, the first quasi-transverse mode was again seen to be independent of angle.

4.3.1.4 TC78-3

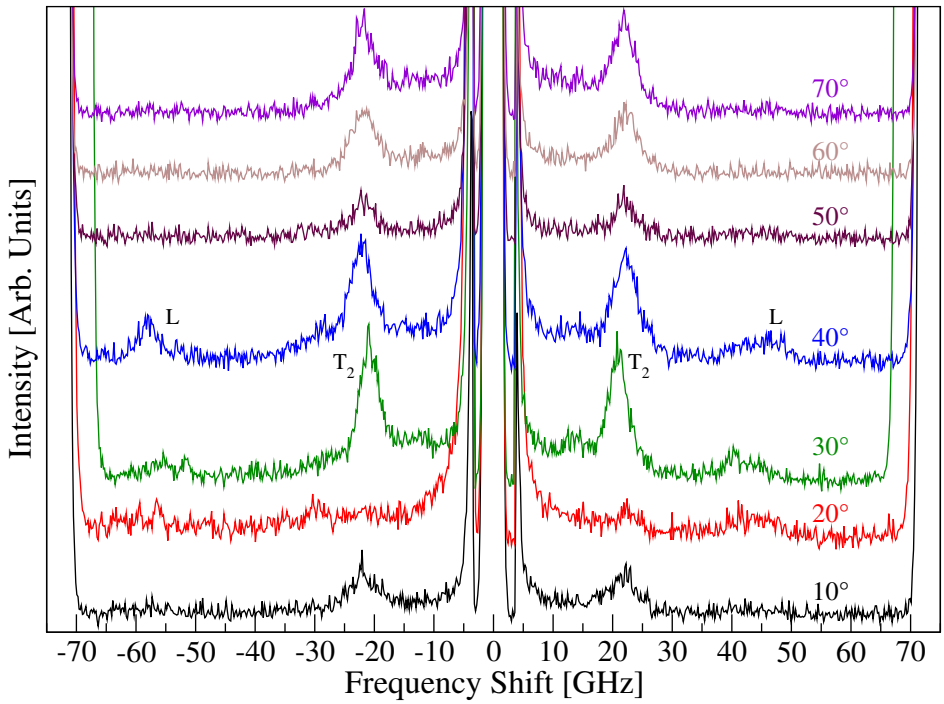

Figure 4.10: Raw Brillouin spectra of TC78 collected at room temperature. T_2 and L correspond to the second quasi-transverse and quasi-longitudinal bulk modes, respectively.

Fig 4.10 presents the spectra of sample T78 collected with θ_i ranging from $10° - 70°$ collected with a FSR of 75 GHz. Here, angular dependence was again found in the second quasi-transverse mode and the observed quasi-longitudinal mode, which appeared when $\theta_i = 30°$ and $\theta_i = 40°$.

4.3.1.5 TC78-4

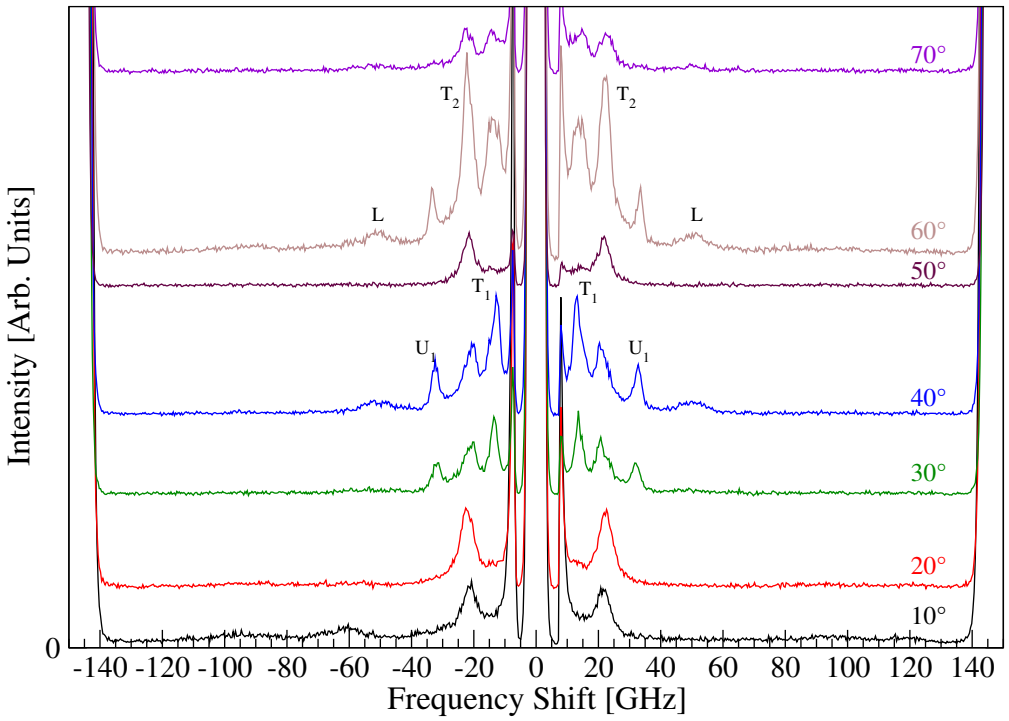

Figure 4.11: Raw Brillouin spectra of TC78 collected at room temperature. T_1, T_2 and L correspond to the quasi-transverse and quasi-longitudinal bulk modes, respectively, and U_1, U_2 correspond to two unknown modes.

Fig 4.11 presents the spectra of sample T78 collected with θ_i ranging from $10° - 70°$ with a FSR of 150 GHz. As before, it was found that both quasi-transverse modes are independent of angle as well as the quasi-longitudinal bulk mode, which has yet to be observed using Brillouin scattering until now. Moreover, two additional modes were also observed and were found to be independent of angle. One was seen at ~ 30 GHz with a strong signal, while the other was seen at ~ 95 GHz and was extremely weak. These two modes are labelled as U_1 and U_2, respectively.

4.3.1.6 TC78-5

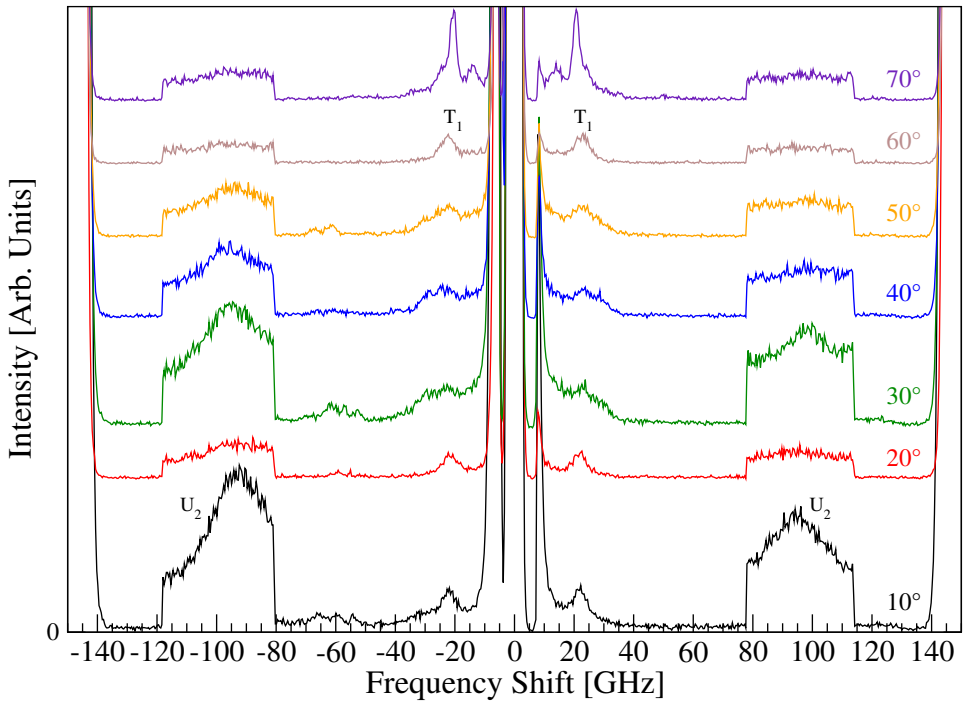

Figure 4.12: Raw Brillouin spectra of sample TC78 collected at room temperature. T_2 and U_2 correspond to the second quasi-transverse and an unknown mode, respectively.

Fig 4.12 presents the spectra of sample T78 collected with θ_i ranging from $10° - 70°$ and an FSR of 150 GHz. Here, the the second unknown mode was investigated by segmenting the region between approximately $80 - 110$ GHz. The observed frequency shifts for U_2 do not appear symmetric, however is expected due to the use of the segmentation window. The average of both Stokes and Anti-Stokes frequency shifts gives the actual frequency shift of the mode which is independent of angle as is the observed quasi-transverse mode.

Table 4.1: Extracted frequency shifts of the Rayleigh surface (R), quasi-transverse (T_1,T_2), quasi-longitudinal (L) and two unknown (U_1,U_2) acoustic phonon modes obtained by Lorentzian fitting.

Sample	θ_i [±1°]	f_R^S [±0.2GHz]	f_R^A [±0.2GHz]	$f_{T_1}^S$ [±0.4GHz]	$f_{T_1}^A$ [±0.4GHz]	$f_{T_2}^S$ [±0.4GHz]	$f_{T_2}^A$ [±0.4GHz]	$f_{U_1}^S$ [±0.2GHz]	$f_{U_1}^A$ [±0.2GHz]	f_L^S [±0.4GHz]	f_L^A [±0.4GHz]	$f_{U_2}^S$ [±0.4GHz]	$f_{U_2}^A$ [±0.4GHz]
T78-1	30	3.9	3.3	-	-	-	-						
(Fig 4.7)	40	4.1	3.6	-	-	-	-	-	-	-	-	-	-
	50	4.6	4.1	-	-	-	-	-	-	-	-	-	-
	60	5.1	4.6	-	-	-	-	-	-	-	-	-	-
	70	5.2	4.7	-	-	-	-	-	-	-	-	-	-
T78-2	10	-	-	15.8	14.7	20.5	20.4	-	-	-	-	-	-
(Fig 4.8)	20	-	-	-	-	21.4	21.4	-	-	-	-	-	-
	30	-	-	14.1	13.2	21.0	20.7	-	-	-	-	-	-
	40	3.1	3.3	13.7	13.7	21.6	21.6	-	-	-	-	-	-
	50	4.0	4.0	14.1	13.2	21.9	21.8	-	-	-	-	-	-
	55	4.5	4.4	15.8	15.2	21.7	21.6	-	-	-	-	-	-
	60	4.6	4.5	14.2	14.1	22.0	21.5	-	-	-	-	-	-
	65	5.0	4.9	13.9	13.3	-	-	-	-	-	-	-	-
	70	5.0	4.9	14.2	14.1	22.0	21.8	-	-	-	-	-	-
	75	5.1	5.1	14.0	13.3	21.7	21.7	-	-	-	-	-	-
T91-1	50	-	4.6	15.8	13.0	-	-	-	-	-	-	-	-
(Fig 4.9)	55	-	4.5	15.8	12.9	-	-	-	-	-	-	-	-
	60	5.2	5.2	15.9	15.0	-	-	-	-	-	-	-	-
	65	5.3	5.2	14.7	14.9	-	-	-	-	-	-	-	-
	70	5.3	5.6	-	-	-	-	-	-	-	-	-	-
T78-3	10	-	-	-	-	21.7	21.6	-	-	-	-	-	-
(Fig 4.10)	20	-	-	-	-	-	-	-	-	-	-	-	-
	30	-	-	-	-	20.8	20.8	-	-	54.6	41.4	-	-
	40	-	-	-	-	22.1	22.0	-	-	57.4	44.8	-	-
	50	-	-	-	-	21.9	22.1	-	-	-	-	-	-
	60	-	-	-	-	21.8	22.2	-	-	-	-	-	-
	70	-	-	-	-	21.8	21.8	-	-	-	-	-	-
T78-4	10	-	-	-	-	21.2	21.4	-	-	-	-	92.9	94.3
(Fig 4.11)	20	-	-	-	-	22.1	22.2	-	-	-	-	-	-
	30	-	-	13.8	13.5	20.9	20.4	31.9	32.0	55.1	48.1	-	-
	40	-	-	13.1	13.4	20.7	20.2	32.4	32.6	50.9	50.2	-	-
	50	-	-	-	-	21.6	21.6	-	-	-	-	-	-
	60	-	-	13.6	13.6	21.9	22.0	33.5	33.4	50.1	50.1	-	-
	70	-	-	14.2	14.7	22.2	22.4	-	-	51.0	50.7	-	-
T78-5	10	-	-	-	-	21.8	22.0	-	-	-	-	92.2	94.8
(Fig 4.12)	20	-	-	-	-	21.5	21.8	-	-	-	-	91.9	94.8
	30	-	-	-	-	-	-	-	-	-	-	94.2	98.1
	40	-	-	-	-	23.5	23.0	-	-	-	-	95.5	99.9
	50	-	-	-	-	22.2	22.5	-	-	-	-	93.8	98.3
	60	-	-	-	-	22.3	22.6	-	-	-	-	97.0	96.8
	70	-	-	-	-	20.7	20.8	-	-	-	-	92.3	97.9

4.3.2 Rayleigh Surface Velocity

By taking the average of both Stokes and Anti-Stokes Rayleigh frequency shifts for each θ_i, the surface Brillouin equation derived in Eqn 4.18 was used to obtain the Rayleigh surface velocity.

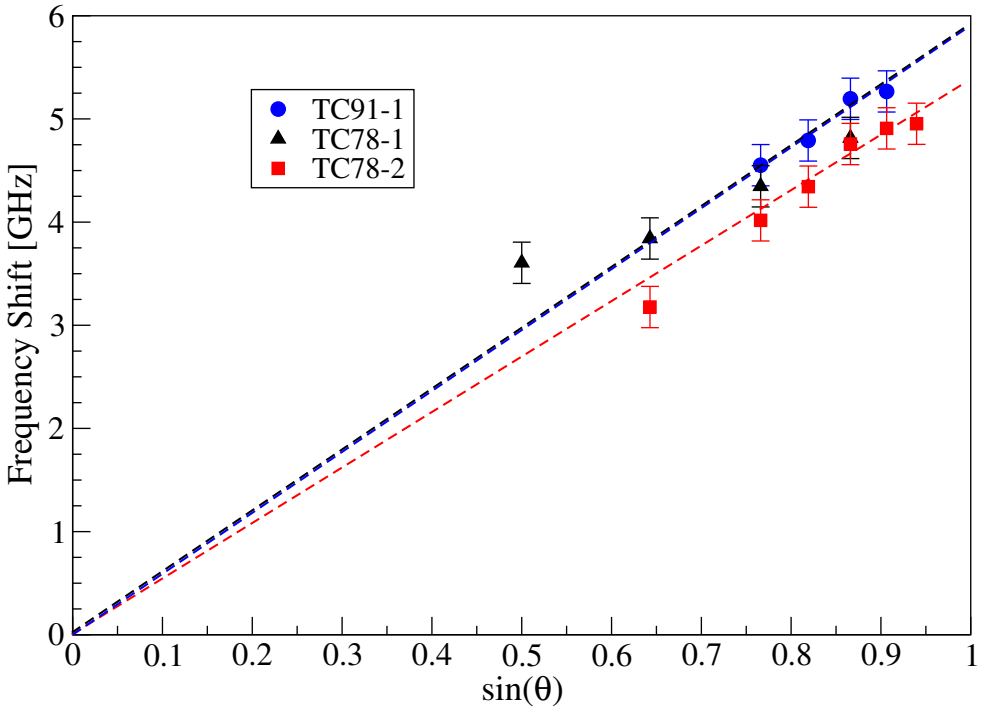

Figure 4.13: The average frequency shift as a function of $\sin\theta_i$ from TC78-1, TC78-2 and TC91-1. Horizontal error bars are the approximate width of data points.

Fig 4.13 presents the frequency shift of the Rayleigh surface mode and its dependence on $\sin\theta_i$ obtained from Table 4.2 for samples TC78 and TC91. Rayleigh surface phonon velocities were obtained by fitting for Eqn 4.14 to the frequency shift verus $\sin\theta_i$ data points for samples TC91-1, TC78-1 and TC78-2.

Table 4.2 presents the Rayleigh surface velocities (v_R) extracted from the slopes of the lines of best fit for samples TC78 and TC91 shown in Fig 4.13 for unknown directions of propagation on the (001) plane, along with surface velocities measured

Table 4.2: Surface Rayleigh velocities for both present and previously completed studies on Bi-2212 at room temperature using Brillouing light scattering. Any work which is presented on different samples which possess the same T_c have been numbered in brackets to avoid confusion.

	T_c [K]	Orientation	v_R [m/s]
Present Work	91 (T91-1)	?	1350±90
	78 (TC78-1)	?	1510±90
	78 (TC78-2)	?	1630±90
[41]	70 (1)	**q** || [100] on (001)	1570
		q || [010] on (001)	1300
	70 (2)	**q** || [100] on (001)	1540
		q || [010] on (001)	1290
	88	**q** || [100] on (001)	1570
		q || [010] on (001)	1320
[27]	?	**q** || [001] on (110)	1525±150
[22]	78-92	**q** || [110] on (001)	1540±66
		q || [100] on (001)	1540±66
		q || [010] on (001)	1540±66
		q || [100] on (010)	1396±97
		q || [001] on (010)	1508±76

from previous Brillouin scattering studies. Rayleigh surface velocities obtained for samples TC78-1 and TC78-2 in the present work were found to agree with one another, however there was a difference of $\sim 8\%$ between the two velocities. Moreover, TC91-1 was not found to agree with either TC78-1 or TC78-2. The weak Rayleigh peaks observed in collected spectra of TC91-1 were a likely contributing factor to the signifcant difference in resulting Rayleigh surface velocities. Moreover, the unknown directions of propagation are also another result for disagreement between the TC78 and TC91 as well as the difference seen in TC78-1 and TC78-2. This is further evidenced in the literature [22], where significant changes are seen in the Rayleigh surface velocity when the propagation direction is varied between [100] and [010] over the (001) plane. Furthermore, when comparing the Rayleigh surface velocity from the literature when **q** || [010] on (001) [22, 41], no agreement was found. This could be attributed to different crystal growth methods, sample impurities or overall sample quality.

4.3.3 Optical Constants of Bi-2212 Using Brillouin Spectra

With collected Brillouin spectra, one can use the Viktorov relation to obtain an estimate of the refractive index which can then be used to calculate the bulk acoustic phonon velocities. The Viktorov relation is given by

$$v_R = \frac{0.87 + 1.12\xi}{1+\xi}\frac{f_T \lambda}{2n}, \tag{4.25}$$

where f_T is the transverse phonon velocity and ξ is the Poisson ratio, equal to 0.2 [36].

The Viktorov relation is an estimate used for isotropic media. While Bi-2212 is not isotropic with the presence of the two doubly degenerate quasi-transverse modes, the refractive index was calculated using the average frequency shift of each of the two modes to create a range of n. With the refractive index obtained, this along with the average full width at half maximum and average frequency shift of each quasi-transverse mode was used in Eqn 4.19 to estimate the range of the extinction coefficient.

Table 4.3 presents the extracted refractive indices and extinction coefficients determined for each quasi-transverse mode, along with the average of both the frequency shifts and full widths obtained by Lorentizan fits for samples TC78 and TC91, where spectra from TC91-1 and TC78-2 were used, respectively. It is noted that before obtaining $\overline{FWHM}$, each full width has 0.280 GHz subtracted from it to account for the instrumental linewidth. This linewidth was obtained by extracting the full width at half maximum of the elastic central peak.

Table 4.3: The average frequency shift ($\bar{f}$) and full width at half maximum ($\overline{FWHM}$) of quasi-transverse bulk modes extracted from collected Brillouin spectra. From each average set, the refractive index and extinction coefficient was calculated and shown.

	$\bar{f}_{T_1}$ [±0.4GHz]	$\overline{FWHM}_{T_1}$ [±0.5GHz]	n_{T_1} [±0.2]	κ_{T_1} [±0.07]	$\bar{f}_{T_2}$ [±0.4GHz]	$\overline{FWHM}_{T_2}$ [±0.4GHz]	n_{T_2} [±0.2]	κ_{T_2} [±0.05]
TC78	14.2	3.6	2.1	0.27	21.5	3.0	3.2	0.22
TC91	14.8	2.8	2.6	0.25	-	-	-	-

As stated above, to account for the degeneracy in the quasi-transverse modes, the average of both n and κ from Table 4.3 is determined for TC78 and the uncertainty

was obtained by extending out to the upper and lower bounds. With the absence of f_{T_2} for TC91, the same uncertainty obtained from TC78 is used. By doing so, the refractive index and extinction coefficient were found to be

$$\begin{aligned} TC78: &\quad n = 2.7 \pm 0.6, \quad \kappa = 0.25 \pm 0.02, \\ TC91: &\quad n = 2.6 \pm 0.6, \quad \kappa = 0.26 \pm 0.02, \end{aligned} \tag{4.26}$$

Using the refractive index and Eqn 3.10 for each sample, the dielectric constants were calculated to be

$$\begin{aligned} TC78: &\quad \epsilon_1 = 7.2 \pm 2, \quad \epsilon_2 = 1.4 \pm 0.4, \\ TC91: &\quad \epsilon_1 = 6.7 \pm 2, \quad \epsilon_2 = 1.4 \pm 0.4. \end{aligned} \tag{4.27}$$

Comparing these results with those obtained in this work from reflectance analysis (refer to Table 3.1), agreement was seen between n, κ, ϵ_1 and ϵ_2. Moreover, agreement was also found between ϵ_2 obtained from Brillouin spectra and the literature [1], for both TC78 and TC91.

4.3.4 Bulk Acoustic Phonon Velocities

With the refractive index now obtained for Bi-2212, the bulk acoustic velocities were calculated using Eqn 4.15 for both quasi-transverse (T_1, T_2), quasi-longitudinal (L) and the two unknown modes (U_1, U_2).

Fig 4.14 presents the bulk acoustic velocities for samples TC91-1, TC78-2, TC78-4 and TC78-5, which were calculated using the refractive index extracted from collected Brillouin spectra shown in Eqn 4.26. The velocities are shown as functions of the phonon propagation direction, θ', as measured away from the [001] direction, where θ' ranged between $4^\circ \sim 21^\circ$ away from the [001] direction. From the figure, velocities were found to be independent of θ' and because of this, both unknown modes were thought to be some type of bulk phenomena since they followed the same behaviour as the quasi-transverse and quasi-longitudinal curves. Moreover, with respect to the first quasi-transverse velocity (v_{T_1}), it was found to be abnormally low for both TC78 and TC91, with v_{T_1} for both samples on the same order as the Rayleigh surface velocity.

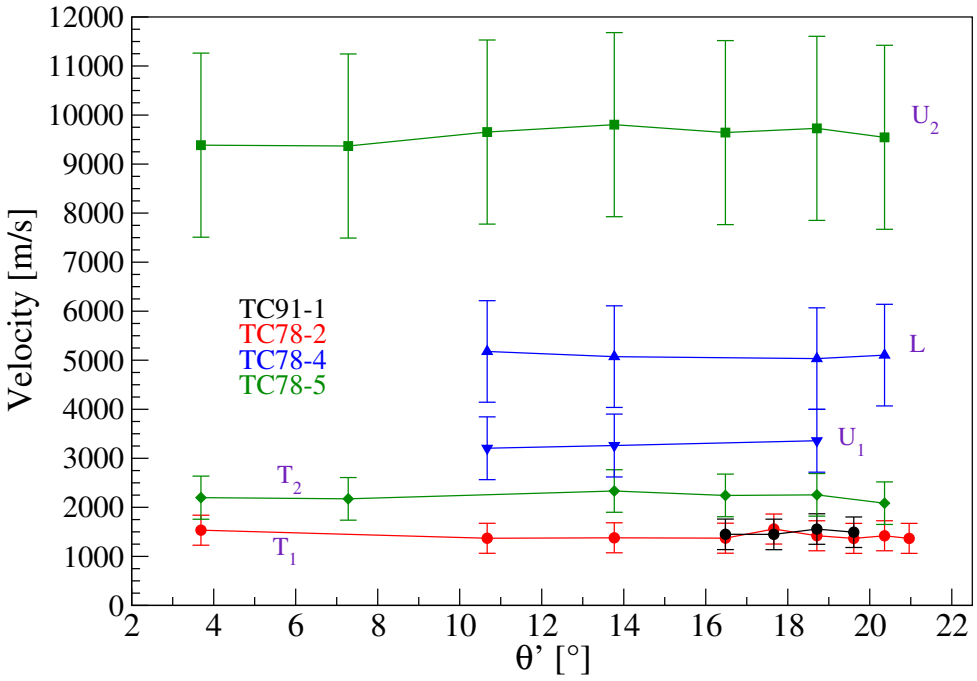

Figure 4.14: Calculated bulk acoustic phonon velocities using the refractive index extracted from collected Brillouin spectra for the quasi-transverse modes (T_1,T_2), quasi-longitudinal mode (L) and two unknown modes which exhibit bulk-like behavior (U_1,U_2). θ' corresponds to measured internal angles away from the [001] direction, which have an uncertainty ranging from $0.5° \sim 4.9°$ over the probed angular range.

Fig 4.15 presents the bulk acoustic velocities for samples TC91-1, TC78-2, TC78-4 and TC78-5, where the refractive index obtained by reflectance analysis and Kramers-Kronig transformations was used along with Eqn 4.26. Compared to Fig 4.14, a smaller internal angular range was probed and slight differences in the velocity curves were observed. Velocities shown in both Figs 4.14-4.15 were found to be independent of θ', the average of each velocity was calculated and used to estimate the bulk velocities for $\mathbf{q} \sim ||$ [001]. These estimates are tabulated in Table 4.4 and include the bulk velocities obtained by previous Brillouin light scattering and ultrasonics studies.

From the Table, it was found that velocities were found to agree with one another, however with n having such a large uncertainty, this was propagated through the velocity calculations resulting in uncertainties of $\sim$ 20%. Comparatively, included

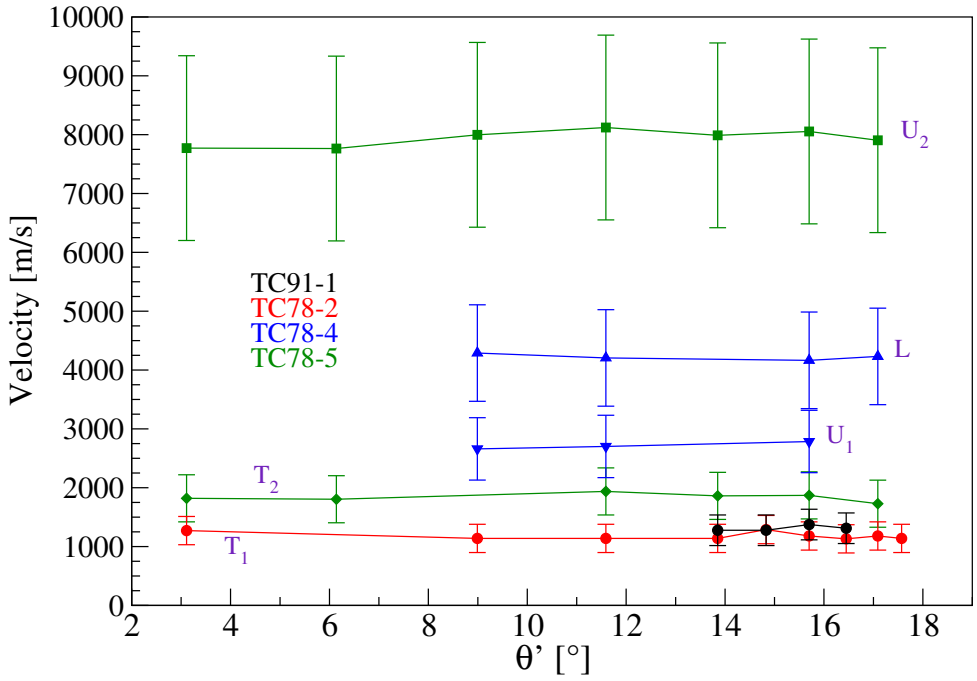

Figure 4.15: Calculated bulk acoustic phonon velocities using the refractive index obtained from reflectance analysis and Kramers-Kronig transformations for the quasi-transverse modes (T_1,T_2), quasi-longitudinal mode (L) and two unknown modes which exhibit bulk-like behavior (U_1,U_2). θ' corresponds to measured internal angles away from the [001] direction, which have an uncertainty ranging from $0.9° \sim 4.7°$ over the probed angular range.

uncertainties from previous work were significantly lower than those seen in present work. For quasi-longitudinal velocities (v_L) presented by previous Brillouin scattering studies [22, 27], these velocities were calculated using the assumption that the observed refractive index independent surface longitudinal resonance mode (v_{LR}) in both studies was approximately equal to v_L. By assuming this, one is inferring that these velocities being measured both parallel perpendicular to the samples surface, respectively, are approximately equal, however this may not be a valid assumption. In contrast, velocities obtained by ultrasonic techniques [3, 5, 15, 16, 44, 45, 46] also do not require knowledge of the refractive index.

When focused on the velocities in the [001] direction, the first quasi-transverse velocity (v_{T_1}) obtained by ultrasonic techniques [5] was found to be in agreement with

Table 4.4: Bulk acoustic phonon velocities collected room temperature for both present work and previously completed studies for Bi-2212. For present work, it is noted in the left-most column which refractive index was used in calculating respective velocities. BLS - Brillouin light scattering, KK - Kramers-Kronig transformations and U - ultrasonics.

	Tc [K]	Orientation	v_{T_1} [m/s]	v_{T_2} [m/s]	v_L [m/s]
Present Work					
BLS					
n_{BLS}	78	$\mathbf{q} \sim \|\|$ [001]	1400±280	2200±400	5100±1020
	91	$\mathbf{q} \sim \|\|$ [001]	1500±300	-	-
n_{KK}	78	$\mathbf{q} \sim \|\|$ [001]	1180±240	1840±370	4220±820
	91	$\mathbf{q} \sim \|\|$ [001]	1310±260	-	-
BLS [22]	78-92	$\mathbf{q} \|\|$ [110] on (001)	-	-	4386±184
	78-92	$\mathbf{q} \|\|$ [001] on (010)	-	-	3413±212
	78-92	$\mathbf{q} \|\|$ [100] on (010)	-	-	4380±194
BLS [27]	?	?	-	-	4650±300
U [3]	?	?	1710±9	-	2464±7
	?	?	1968±10	-	3330±10
U [44]	74	?	1735	-	2846
U [15, 16]	84	[100]	-	-	4320
		[010]	-	2762	4097
		[110]	-	-	4647
U [45, 46]	84.5	[100]	-	-	4580
		[010]	-	-	4130
		[010]	-	2460	-
U [5]	?	[001]	1750±10	-	2670±10
		?	1740±10	2460±10	4370±10
		45° from (110)	2150±10	-	3430±10

v_{T_1} calculated using n_{BLS} in the present work. Moreover, ultrasonic measurements of v_L [5] in the [001] direction was not found to agree with either present work or that obtained by v_{LR} assumptions [22], while the velocity obtained by this assumption

agreed with v_L calculated using n_{KK}.

Comparing the remaining velocities with those obtained in the present work, it was determined that velocities were found to be highly variant. This was attributed to sample differences between each study, where sample quality and the presence of impurities can greatly affect measurements. There was also a lack of sample and crystallographic information presented in previous work. The exact T_c of studied samples was missing in some work [3, 5, 22, 27] as well as a direction [3, 5, 27, 44].

Chapter 5

Conclusion

5.1 Concluding Remarks

The optical properties were determined by experimental analyses on three bulk Bi-2212 crystals, each with a T_c of 78 K, 90 K and 91 K, each labelled TC78, TC90 and TC91, respectively. Reflectance imaging of each crystal was first performed and using these images along with the Kramers-Kronig transformations, the first estimate of the complex refractive index was determined to be $\tilde{n} = 3.2{+}0.16i$ for TC78 and TC90, and $\tilde{n} = 3.0 + 0.14i$ for TC91. The reflectance images were also used alongside a modified optical contrast method to obtain a secondary estimate via reflectance analysis. This method was not pursued further, however, as the mathematical model used did not appear to describe the sample-substrate system imaged. The complex refractive index of each sample was then used to calculate the complex dielectric function, which was found to be $\tilde{\epsilon} = 9.6 + 1.0i$ for TC78 and TC90, and $\tilde{\epsilon} = 9.0 + 0.9i$ for TC91. It was determined that the real part of the dielectric function was almost three times that of previously recorded values, while the imaginary part was in agreement.

Brillouin light scattering experiments were performed on samples TC78 and TC91 at room temperature. From collected spectra, a total of six acoustic modes were observed; the Rayleigh surface mode, two quasi-transverse bulk modes, and the quasi-longitudinal bulk mode. Two unknown modes were also observed in the spectra collected on TC78. While probed from $3^\circ \sim 21^\circ$ from the [001] direction, the three bulk mode velocities were found to be independent of the angle, as were the unknown

modes, suggesting some type of bulk phenomena. The Rayleigh surface velocity for was found to be 1630 ± 90 m/s and 1350 ± 90 m/s for samples TC78 and TC91, respectively, in an unknown direction on the (001) plane.

Using the Rayleigh surface velocities as well as the frequency shifts and line-widths, a second estimate of the complex refractive index for each sample was extracted using collected Brillouin spectra, giving $\tilde{n} = 2.7 + 0.25i$ and $\tilde{n} = 2.6 + 0.26i$ for TC78 and TC91, respectively. These were again used to estimate the complex dielectric function, found to be $\tilde{\epsilon} = 7.2 + 1.3i$ and $\tilde{\epsilon} = 6.7 + 1.4i$, respectively.

The estimates for the refractive index obtained by both Brillouin peak relations and from reflectance and Kramers-Kronig analysis were then used to calculate the bulk acoustic velocities for the three bulk modes and two unknown bulk-like modes. Bulk velocities were found to range between $(1180 - 1400) \pm 270$ m/s, $(1840 - 2200) \pm 290$ m/s and $(4220 - 5100) \pm 920$ m/s for the two quasi-transverse and quasi-longitudinal modes, respectively, for TC78 while the first quasi-transverse mode was found be $(1310 - 1500) \pm 280$ m/s for TC91. These velocities appeared in the range of those obtained by previous Brillouin scattering and ultrasonic studies, however many published works omitted crystallographic and sample information, making comparison difficult. Moreover, the velocities of the two unknown bulk-like modes in TC78 were found to be $(3270 - 4070) \pm 580$ m/s and $(7940 - 9590) \pm 1720$ m/s.

In order to make better conclusions on the bulk phonon velocities using Brillouin scattering, the error in the refractive index must be reduced. This may be done by collecting a large volume of spectra over multiple directions and obtaining an average of the extracted refractive index. Bi-2212 samples of differing doping may also be studied, where one may be able to map how the quasi-transverse modes degenerate.

5.2 Future Work

There are many additional directions to go in for extending this work. Firstly, the degeneracy in the acoustic quasi-transverse modes may be investigated in order to obtain a better estimate of the refractive index and in turn, the acoustic phonon velocities. Moreover, performing optical contrast on appropriately deposited Bi-2212 crystals may also help to obtain better estimates of the still disputed optical constants.

The nature of the two bulk-like unknown modes is another path which may be investigated. The first thing one may do is polarize the light to determine whether the peaks are due to transverse or longitudinal modes. Furthermore, Bi-2212 is very complex, and the nature of these modes could be due to some other phenomenon such as plasmons, which were not in the scope of this particular study.

Bibliography

[1] I. Bozovic. Plasmons in Cuprate Superconductors. *Phys. Rev. B*, 42:1969–1984, 1990.

[2] C. S. Lim, L. Wang, C. K. Chua, Z. Sofer, O. Jankovský . High Temperature Superconducting Materials as Bifunctional Catalysts for Hydrogen Evolution and Oxygen Reduction. *J. Mater. Chem. A*, 3:8346–8352, 2015.

[3] C. Y. Chu, J. L. Routbort, N. Chen, A. C. Biondo, D. S. Kupperman and K. C. Goretta. Mechanical Properties and Texture of Dense Polycrystalline $Bi_2Sr_2CaCuO_x$. *Supercond. Sci. Tech.*, 5(5):306–312, 1992.

[4] D. Bing, Y. Wang, J. Bai, R. Du, G. Wu and L. Liu. Optical Contrast for Identifying the Thickness of Two-Dimensional Materials. *Opt. Commun.*, 406:128–138, 2018.

[5] F. Chang, P.J. Ford, G.A. Saunders, L. Jiaqiang, D.P. Almond, B. Chapman, M. Cankurtaran, R.B. Poeppel and K.C. Goretta. Anisotropic Elastic and Nonlinear Acoustic Properties of Very Dense Textured $Bi_2Sr_2CaCu_2O_{8+y}$. *Supercond. Sci. Tech.*, 6(7):184–189, 1993.

[6] S. Fujita and S. Godoy. Theory of High Temperature Superconductivity. Kluwer Academic Publishers. 2001.

[7] J. Ashkenazi, S. E. Barnes, F. Zuo, G. C. Vezzoli and B. M. Klein. High-Temperature Superconductivity: Physical Properties, Microscopic Theory, and Mechanisms. Springer Publishing. 1992.

[8] J. Bechhoefer. Kramers-Kronig, Bode and the Meaning of Zero. *ArXiv:1107.0071*, 2011.

[9] J. Dominec. Ultrasonic and Related Experiments in High-Tc Superconductors. *Supercond. Sci. Tech.*, 6(3):153–172, 1993.

[10] J. Henrie, S. Kellis, S. M. Schultz and A. Hawkins. Electronic Color Charts for Dielectric Films on Silicon. *Opt. Express*, 12(7):1464–1469, 2004.

[11] J. Hu, S. Zhang, Q. Zhang, W. Cai, D. Tingzhang, Z. Liangkun, Y. He and J. Xiang. Ultrasonic Attenuation and Velocity in BiSrCaCuO High Tc Superconductor. *Physica C*, 162-164:444–445, 1989.

[12] J. Hwang, T. Timusk and G. D. Gu. Doping Dependent Optical Properties of $Bi_2Sr_2CaCuO_{8+\delta}$. *ArXiv:0607653v2*, 2006.

[13] J. Kobayashi, T. Asahi, M. Sakurai, M. Takahashi, K. Okubo and Y. Enomoto. Optical Properties of Superconducting $Bi_2Sr_2CaCuO_8$. *Phys. Rev. B*, 53:11784–11795, 1996.

[14] J. Konstantinović, G. Parette, Z. Djordjević and A. Menelle. Structural Transformations of the $YB_2Cu_3O_{6.84}$ Crystal Lattice in the Temperature Interval 9 K to 300 K. *Solid State Commun.*, 70(2):163–166, 1989.

[15] J. Wu, Y. Wang, H. Shen and J. Zhu. Ultrasonic Study of the Soft Phonon Mode in $Bi_2Sr_2CaCu_2O_8$ Single Crystals. *Phys. Lett. A*, 148(1-2):127–130, 1990.

[16] J. Wu, Y. Wang, P. Guo, H. Shen. Elastic Constants and Observation of Significant Elastic Softening in Superconducting $Bi_2Sr_2CaCu_2O_8$ Single Crystals. *Phys. Rev. B*, 47(5):2806–2811, 1993.

[17] T. Jacobs. Unraveling the Cuprate Superconductor Phase Diagram: Intrinsic Tunneling Spectroscopy and Electrical Doping. *Doctoral Thesis, Stockholm University, Sweden*, 2016.

[18] C. Kittel. Introduction to Solid State Physics - 8th Edition. Wiley Publisher. 2004.

[19] L. J. Sandilands, A. A. Reijnders, A. H. Su, V. Baydina, Z. Xu, A. Yang, G. Gu, T. Pedersen, F. Borondics and K. S. Burch. Origin of the Insulating State in Exfoliated High-Tc Two-Dimensional Atomic Crystals. *Phys. Rev. B*, 90:081402, 2014.

[20] L. Sihan, H. Yusheng, W. Chongde and S. Zhaohui. Elastic Constants of Single-Phase $Bi_2Sr_2CaCu_2O_{8+y}$ Superconductor. *Supercond. Sci. Tech.*, 2(2):145–148, 1990.

[21] M. A. Quijada, D. B. Tanner, R. J. Kelley, M. Onellion, H. Berger and G. Margaritondo. Anisotropy in the ab-Plane Optical Properties of $Bi_2Sr_2CaCuO_8$ Single-Domain Crystals. *Phys. Rev. B*, 60(21):14917–14934, 1999.

[22] M. Boekholt, J.V. Harzer, B. Hillebrands and G. Güntherodt. Determination of the Sound Velocities and the Complete Set of Elastic Constants for $Bi_2Sr_2CaCu_2O_{8+\delta}$ Single Crystals Using Brillouin Light Scattering. *Physica C*, 179:101–106, 1991.

[23] M. G. Kanatzidis, R. Pöttgen and W. Jeitschoko. The Metal Flux: A Preparative Tool for the Exploration of Intermetallic Compounds. *Angew. Chem. Int. Edit.*, 44(43):6996–7023, 2005.

[24] M. Saint-Paul and J.L. Tholence. Sound Velocity in $Bi_2Sr_2CaCu_2O_8$ Single Crystals. *Physica C*, 166(5-6):405–407, 1990.

[25] M. P. Marder. Condensed Matter Physics - 2nd Edition. Wiley Publisher. 2010.

[26] A. Mourachkine. High Temperature Superconductivity in Cuprates - the Nonlinear Mechanism and Tunneling Measurements. Kluwer Academic Publishers. 2002.

[27] P. Baumgart, S. Blumenröder, A. Erle, B. Billebrands, P. Splittgerber, G. Güntherodt and H. Schmidt. Sound Velocities of $YBa_2Cu_3O_{7-\delta}$ and $Bi_2Sr_2CaCu_2O_x$ Single Crystals Measured by Brillouin Spectroscopy. *Physica C*, 192-164:1073–1074, 1989.

[28] P. Lemmens, F. Stellmach, J. Wynants, S. Ewert, A. Comberg, H. Passing and G. Marbach. Acoustic Measurements on High-Tc Superconductors in the Systems Y-Ba-Cu-oO and Bi,Pb-Sr-Ca-Cu-O. *J. Less. Common. Met.*, 151:153 – 158, 1989.

[29] D. Pascale. A Review of RGB Color Spaces From xyY to R'G'B'. *The Babel Color Company*, 2002.

[30] H. R. Phillip and E. A. Taft. Kramer-Kronig Analysis of Reflectance Data for Diamond. *Phys. Rev. A*, 136:1445–1448, 1964.

[31] V. Plecháček and J. Dominec. Sound Velocities in Single-Phase 2223 Bi, Pb-Sr-Ca-Cu-O Polycrystalline Superconductor. *Solid State Commun.*, 74(7):633–635, 1990.

[32] A. Polumska. Elastic Properties of Porous Silicon Superlattices. *Doctoral Thesis, Memorial University of Newfoundland, Canada*, 2010.

[33] A. D. Rakić. Algorithm for the Determination of Intrinsic Optical Constants of Metal Films: Application to Aluminum. *Appl. Optics*, 34(22):4755–4767, 1995.

[34] L. Rayleigh. On Waves Propagated along the Plane Surface of an Elastic Solid. *P. Lond. Math. Soc.*, 17:4–11, 1885.

[35] P. V. Reddy and S. Shekar. Ultrasonic Studies of Some Bi-Based High-Tc Superconductors. *Supercond. Sci. Tech.*, 6(11):785–789, 1993.

[36] S. K. Sahu, D Jangade, A. Thamizhavel, M. M. Deshmukh and V. Singh. Elastic Properties of Few Unit Cell Thick Superconducting Crystals of $Bi_2Sr_2CaCuO_8$. *ArXiv:1910.02221v1*, 2019.

[37] J. R. Sandercock. Brillouin-Scattering Measurements on Silicon and Germanium. *Phys. Rev. Lett.*, 28:237–240, 1972.

[38] T. P. Sheahen. Introduction to High Temperature Superconductivity. Kluwer Academic Publishers. 1994.

[39] S. H. Simon. The Oxford Solid State Basics. Oxford University Press. 2013.

[40] S. Spencer. Phonon Dynamics of Ceramic $PbSc_{0.5}Ta_{0.5}O_3$. *Masters Thesis, Memorial University of Newfoundland, Canada*, 2016.

[41] V. V. Aleksandrov, T. S. Velichkina, V. I. Voronkova, A. A. Gippius, S. V. Rek'ko, I. A. Yakovlev and V. K. Yanovskii. Bi-Based Superconductors and Their Surface Wave Velocities. *Solid State Commun.*, 76(5):685–689, 1990.

[42] W. Ouyang, X. Liu, Y. Zhang, J. Yang and Q. Zheng. Optical Methods for Determining Thicknesses of Few-Layer Graphene Flakes. *Nanotechnology*, 24(50):505701, 2013.

[43] Y. Huang, E. Sutter, N. N. Shi, J. Zheng, T. Yang, D. Englund, H. Gao and P. Sutter. Reliable Exfoliation of Large-Area High-Quality Flakes of Graphene and Other Two-Dimensional Materials. *ACS Nano*, 9(11):10612–10620, 2015.

[44] Y. S. He, J. Xiang, F. G. Chang, J. C. Zhang, A. S. He, H. Wang and B. L. Gu. Anomalous Structural Changes and Elastic Properties of Bismuth Oxide Superconductors. *Physica C*, 162-164:450–451, 1989.

[45] Y. Wang, J. Wu, J. Zhu, H. Shen, J. Z. Zhang, Y. F. Yang and Z. X. Zhao. Ultrasonic Study on Anisotropic Elasticity of $Bi_2Sr_2CaCu_2O_8$ Single Crystal. *Beijing International Conference on High Temperature Superconductivity*, 22:426, 1989.

[46] Y. Wang, J. Wu, J. Zhu, H. Shen, Y. Yan and Z. Zhao. Ultrasonic Study on Structural Instability of $Bi_2Sr_2CaCu_2O_8$ Single Crystal. *Physica C*, 162-164:454–455, 1989.

Appendix A

Preliminary Brillouin Spectra

A.1 Bi-2212 Anisotropy

Additional crystallographic information was attempted to be obtained. By holding θ_i constant at 50° and rotating sample TC78 with respect to its azimuthal angle θ_z, the expected periodicity in resulting frequency shifts can allow for one to extract information on the (100), (010) and (001) planes.

Fig A.1(a) presents the spectra collected for rotating the azimuthal angle $0° - 120°$ with respect to the arbitrarily chosen starting angle. From the figure, it was hard to discern small changes in resulting frequency shifts since the resolution was so poor. Moreover, during collection, the sample had fallen off the sample mount. Once this happened, it was remounted and collection ensued with θ_z ranging from $0° - 70°$ with respect to a newly chosen arbitrary starting angle.

Fig A.1(b) presents the second set of spectra collected with θ_z ranging from $0° - 70°$, with extracted frequency shifts via Lorentzian fitting from both figures shown in Table A.1. To gain a better understanding of the periodicity, one should collect data over an angular range of at least 180°, however with alignment issues and long collection times, this was not doable within the limited time frame.

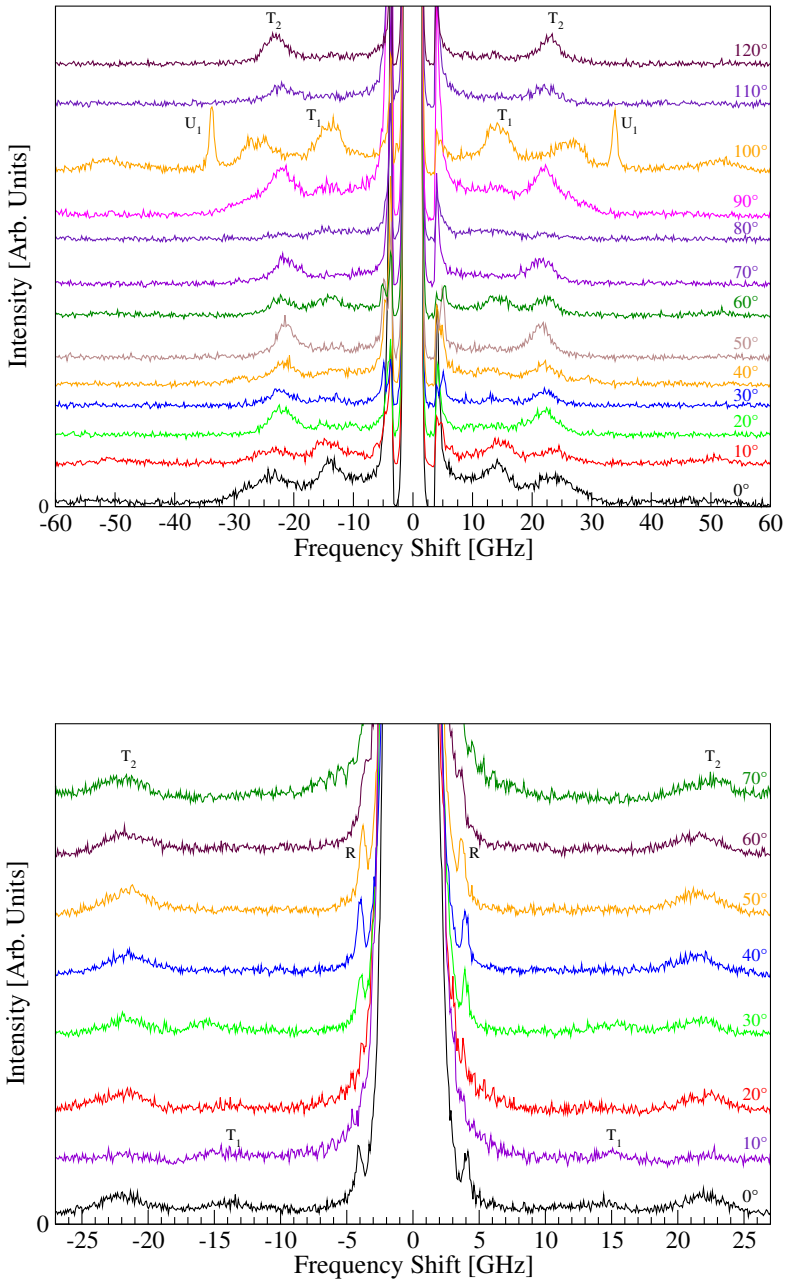

Figure A.1: Raw Brillouin spectra of sample TC78 at room temperature with θ_i held constant at 50° and θ_z varied from (a) $0° - 120°$ with a FSR of 80 GHz and (b) $0° - 70°$ with an FSR of 30 GHz.

Table A.1: Extracted frequency shifts of the Rayleigh surface (R), quasi-transverse (T_1,T_2), quasi-longitudinal (L) and unknown bulk-like (U_1) acoustic phonon modes obtained by Lorentzian fitting.

	θ_z [$\pm1°$]	f_R^S [$\pm$0.2GHz]	f_R^A [$\pm$0.2GHz]	$f_{T_1}^S$ [$\pm$0.4GHz]	$f_{T_1}^A$ [$\pm$0.4GHz]	$f_{T_2}^S$ [$\pm$0.4GHz]	$f_{T_2}^A$ [$\pm$0.4GHz]	$f_{U_1}^S$ [$\pm$0.2GHz]	$f_{U_1}^A$ [$\pm$0.2GHz]	f_L^S [$\pm$0.3GHz]	f_L^A [$\pm$0.3GHz]
Fig A.1(a)	0	-	-	13.8	13.8	23.2	23.5	-	-	53.6	44.8
	10	-	-	14.3	14.4	23.1	23.3	-	-	49.6	49.5
	20	-	-	-	-	21.9	21.8	-	-	-	-
	30	-	-	14.1	14.3	22.1	22.0	-	-	-	-
	40	-	-	12.5	12.6	21.5	21.9	28.9	29.0	-	-
	50	-	-	13.8	14.0	22.0	22.2	-	-	-	-
	60	-	-	13.8	14.0	22.0	22.2	-	-	51.4	50.5
	70	-	-	-	-	21.3	21.5	-	-	-	-
	80	-	-	13.3	11.9	22.2	22.2	-	-	-	-
	90	-	-	14.2	13.8	21.9	22.0	-	-	-	-
	100	-	-	13.9	14.2	26.0	26.2	33.8	33.9	50.5	51.4
	110	-	-	-	-	22.0	22.0	-	-	-	-
	120	-	-	13.2	13.2	23.0	22.9	-	-		
Fig A.1(b)	0	4.0	4.0	14.0	13.6	21.9	21.9	-	-	-	-
	10	-	-	14.4	14.9	21.9	22.2	-	-	-	-
	20	-	-	13.8	13.7	22.1	22.1	-	-	-	-
	30	4.0	3.9	15.6	15.3	21.6	21.6	-	-	-	-
	40	4.0	4.0	-	-	21.4	21.3	-	-	-	-
	50	3.9	3.6	-	-	21.5	21.4	-	-	-	-
	60	-	-	-	-	21.5	21.3	-	-	-	-
	70	-	-	-	-	22.2	22.6	-	-	-	-

Using frequency shifts in Table A.1, Fig A.2 presents the second quasi-transverse modes from (b) as a function of θ_z. With a small angular range obtained, no planar information was able to be obtained, however this analysis further proved the anistropic nature of sample TC78, as periodicity was found along with agreement in a sinusoidal fit.

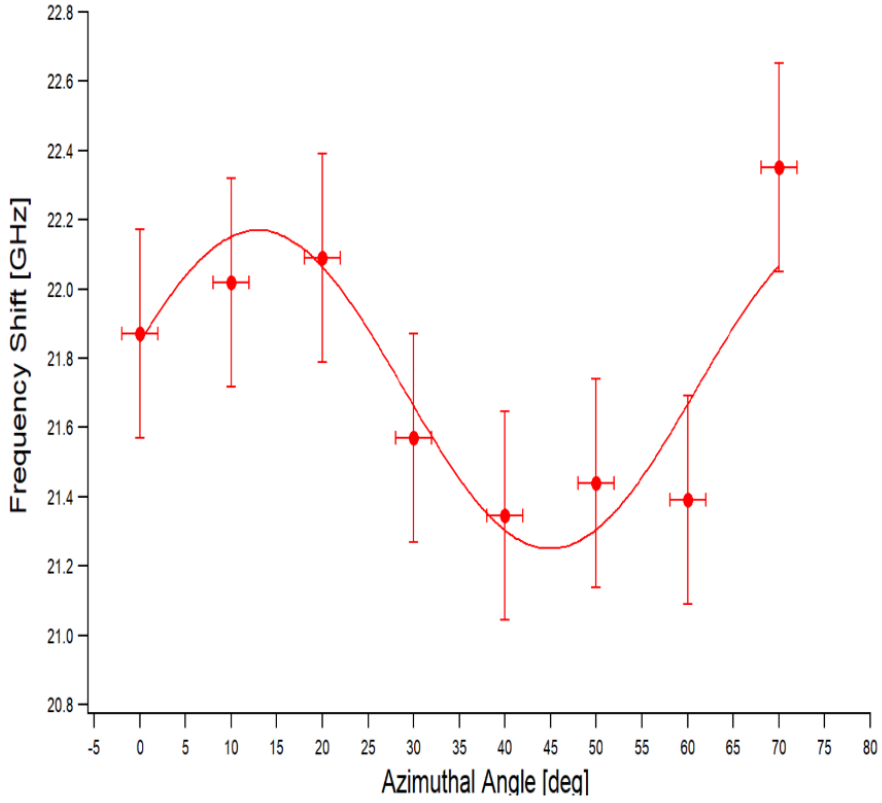

Figure A.2: Extracted quasi-transverse frequency shifts from Fig A.1(b) as a function of the azimuthal angle, θ_z. Periodic nature was observed, however more data is required for further analysis on determining additional information on the crystallographic planes.

Appendix B

Reflectance and Optical Contrast Scripts

B.1 Reflectance Image Rebinning

Below is the script written to analyze collected reflectance images via the rebinning routine described in Chapter 3.

```
from __future__ import division
from PIL import Image
import numpy as np
import matplotlib.pyplot as plt



#Import reflectance image and initializing image size
imgload = Image.open('semmountbscco-10x_532_V12_2.jpg')
pix = imgload.load()
x,y = imgload.size
img=np.zeros((x,y))

#Creating bins for each of the 255 channels
binnum=np.zeros((255))
imgsize=x*y
```

```
binned_xy_coords=[]
bin_collect=[]

#Determining number of counts in each channel by scanning each pixel site
for r in xrange(255):
    for j in xrange(y):
        for i in xrange(x):
            img[i][j]=pix[i,j][1]
            if r==pix[i,j][1]:
                binnum[r]=binnum[r]+1
                bin_collect.append((i,j))
    binned_xy_coords.append(bin_collect)
    bin_collect=[]

dat=[]

#Plotting channel distribution
histdat=np.zeros((255,2))
for i in xrange(255):
    histdat[i]=[i,binnum[i]]
    dat.append((i,binnum[i]))
plt.xlim(0,150)
plt.bar(histdat[:,0],histdat[:,1])

data=[]

#Storing the positions according to each channel
for k in xrange(len(binnum)):
    for l in xrange(len(binned_xy_coords[k])):
        data.append((k,binned_xy_coords[k][l][0],binned_xy_coords[k][l][1]))

np.savetxt('SampleImg_0255hist.dat',dat)
np.savetxt('SampleImg_xycoords.dat',data,fmt='%.5e')

#Import positions corresponding to channel value
dat=np.genfromtxt('SampleImg_xycoords.dat',delimiter=' ',skip_header=0)
```

```
binorigin = dat[:,0]
x_position = dat[:,1]
y_position = dat[:,2]

#Initialize new array for new partitioned bin
newbin=np.zeros((len(binorigin),1,3))
partition=3 # new bin partitions
maxsize=254/partition+1

index=0
binarray=np.zeros((255,2))
for a in range(0,255):
    count=a%partition
    binarray[a]=index,a
    if count==partition-1:
        index+=1

dat=[]
counts=0

#Rebinning the 255 channels into bins of 3
for a in range(0,255):
    for b in range(0,len(binorigin)):
        if binorigin[b]==a:
            dat.append(( a,binarray[a][0],x_position[b],y_position[b] ))

np.savetxt('SampleImg_xycoords_rebin.dat',dat,fmt='%.5e')

dat = np.genfromtxt('SampleImg_xycoords_rebin.dat', delimiter=' ',skip_header=0)
binorigin = dat[:,0]
newbin = dat[:,1]
x_position = dat[:,2]
y_position = dat[:,3]

storingbin=np.zeros((len(binorigin),2))

data=[]
```

```
for a in range(0,51):
    for b in range(0,len(newbin)):
        storingbin[a][1]=a
        if a==newbin[b]:
            storingbin[a][0]+=1
    data.append((storingbin[a][0],storingbin[a][1]))

red=0
redcount=0
green=0
greencount=0
white=0
whitecount=0
blue=0
bluecount=0

#Define each rebinned bin with a new color
for i in range(0,len(newbin)):

    if newbin[i]<7:
        pix[x_position[i],y_position[i]]=(255,255,255,255)
        white+=binorigin[i]
        whitecount+=1
    if newbin[i]==9 or newbin[i]==10:
        pix[x_position[i],y_position[i]]=(100,0,0,255)
        red+=binorigin[i]
        redcount+=1
    if newbin[i]==8:
        pix[x_position[i],y_position[i]]=(0,100,0,255)
        green+=binorigin[i]
        greencount+=1
    if newbin[i]==7:
        pix[x_position[i],y_position[i]]=(0,0,150,255)
        blue+=binorigin[i]
        bluecount+=1
    if newbin[i]<=22:
        pix[x_position[i],y_position[i]]=(255,0,0,255)
```

```
    if newbin[i]==34:
        pix[x_position[i],y_position[i]]=(0,0,150,255)
        red+=binorigin[i]
        redcount+=1
    if newbin[i]==33:
        pix[x_position[i],y_position[i]]=(0,0,255,255)
        red+=binorigin[i]
        redcount+=1
    if newbin[i]==32:
        pix[x_position[i],y_position[i]]=(0,0,100,255)
        red+=binorigin[i]
        redcount+=1
    if  newbin[i]==31:
        pix[x_position[i],y_position[i]]=(0,255,0,255)
        green+=binorigin[i]
        greencount+=1
    if newbin[i]==30:
        pix[x_position[i],y_position[i]]=(0,255,0,255)
        green+=binorigin[i]
        greencount+=1
    if newbin[i]==29:
        pix[x_position[i],y_position[i]]=(0,255,0,255)
        green+=binorigin[i]
        greencount+=1
imgload.show()
imgload.save("Sampleimage_rebinned.jpg")
```

B.2 Optical Contrast

Below is the modified optical contrast script written to extract the refractive index and extinction coefficient.

```
from __future__ import division
import numpy as np
```

```
import math
import cmath


OC_calc=0
lamb=532e-9 #Wavelength [m]


#complex refractive index of air
n0=1.000274+0j

#complex refractive index of carbon tape
n2=2.42+0j

#complex refractive index of aluminum sample holder
n3=2.6913+1.4557*1j

#measured thickness of Bi-2212
d1=8.782e-6

#measured thickness of carbon tape
d2=51.79e-6


#defining reflection coefficients and second phase
r02=(n0-n2) / (n0+n2)
r23=(n2-n3) / (n2+n3)
phi2=(2*math.pi*n2*d2)/(lamb)
r0=( r02 + r23*cmath.exp(-2*1j*phi2) ) / ( 1 + r02*r23*cmath.exp(-2*1j*phi2) )

#number of iterations for extinction coefficient
k=np.empty([125000])

N=[]

#OC value obtained from experimentally
SEM_OC=0.328312412831
```

```
#initialzing tolerance for accepted OC values
uncertainty=SEM_OC*1e-4
SEM_OC_upper=SEM_OC+uncertainty
SEM_OC_lower=SEM_OC-uncertainty

for i in range(len(k)):
    if(i==0):
        k[0]=1e-4
    else:
        k[i]=k[i-1]+7e-6
for n in np.arange(1,6,0.01):
    for i in range(len(k)):
        n1=n+1j*k[i]
        r01=(n0-n1) / (n0+n1)
        r12=(n1-n2) / (n1+n2)
        phi1=(2*math.pi*n1*d1)/(lamb)

    #catching any division by zero or overflow errors
        try:
            r=( r01 + r01*r12*r23*cmath.exp(-2*1j*phi2) + r12*cmath.exp(-2*1j*phi1) + r23*
            R0=abs(r0**2)
            R=abs(r**2)
            C=(R0-R)/R0
        except OverflowError:
            C=0
        if(abs(C) < abs(SEM_OC_upper) and abs(C) > abs(SEM_OC_lower)):
            N.append((n,k[i],FreqRatio))
            print n,k[i], C

np.savetxt('SEMmountBSCCO-532-nk-OC.dat',N)
```

B.3 Kramers-Kronig Phase Calculation

Below is the script written to evaluate the integral transformation shown in Eqn 3.17 using the boundary conditions provided in Eqn 3.16.

```
from __future__ import division
from scipy import integrate
import math
import numpy as np
import time
start_time = time.time()

x1=10864.28; x2=24599.91; omegafixed=18796

def R1(omega):
    return 0.61144*omega+.91563

def R2(omega):
    return .015086*omega+0.085441

def R3(omega):
    return 0.0035039*omega+0.18498

def R(omega):
    if omega < x1:
        return R1(omega)
    if omega > x1 and omega < x2:
        return R2(omega)
    if omega > x2:
        return R3(omega)

def integrand(omega, omegaprime):
   return ( np.log(R(omegaprime))-np.log(R(omega)) )/(omega**2 - omegaprime**2)

wpmin=0
wpmax=25000
wgrid=1
```

```
wpstep=(wpmax-wpmin)/wgrid

data=[]
sum=0
w=18796.99248

for x in np.arange(wpmin,wpmax,wpstep):
    sum+=wpstep*integrand(w,x)
    data.append((w,(w/math.pi)*sum ))

print (w/math.pi)*sum
np.savetxt('thetaconverge.dat',data)
```